Numerical study of droplet deformation in shear flow using a conservative level-set method

Ahmad Amani[a,*], Néstor Balcázar[b], Jesús Castro[a], Assensi Oliva[a,*]

[a] *Heat and Mass Transfer Technological Center (CTTC)*
Polytechnic University of Catalonia (UPC), Terrassa (Barcelona), Spain
http://www.cttc.upc.edu
[b] *Termo Fluids S.L.*
Avda Jacquard 97 1-E, 08222 Terrassa (Barcelona), Spain
http://www.termofluids.com

Abstract

This paper is concerned with a numerical study on the behavior of a single Newtonian droplet suspended in another Newtonian fluid, all subjected to a simple shear flow. Conservative finite-volume approximation on a collocated three-dimensional grid along with a conservative Level-set method are used to solve the governing equations. Four parameters of capillary number (Ca), Viscosity ratio (λ), Reynolds number (Re) and walls confinement ratio are used to physically define the problem. The main focus of the current study is to investigate the effect of viscosity on walls critical confinment ratio. In this paper, the phrase critical is used to specify a state of governing parameters in which divides the parameter space into the subcritical and supercritical regions where droplets attain a steady shape or breakup, respectively. To do so, first, we validate the ability of proposed method on capturing the physics of droplet deformation including: steady-state subcritical deformation of non-confined droplet, breakup of supercritical conditioned droplet, steady-state deformation of moderate confined droplet, subcritical oscillation of highly-confined droplet, and the effect of viscosity ratio on deformation of the droplet. The extracted results are compared with available experimental, analytical and numerical data from the literature. Afterward, for a constant capillary number of 0.3 and a low Reynolds number of 1.0, subcritical (steady-state) and supercritical (breakup) deformations of the droplet for a wide range of walls confinement in different viscosity ratios are studied. The results indicate the existence of two steady-state regions in a viscosity ratio-walls confinement ratio graph which are separated by a breakup region.

Keywords: Simple shear flow, Droplet deformation and breakup, Conservative Level-set method, Viscosity ratio, Critical confinement ratio

*Corresponding author
Email addresses: ahmad@cttc.upc.edu.com (Ahmad Amani), nestor@cttc.upc.edu (Néstor Balcázar),

1. Introduction

Droplets of one liquid dispersed in an immiscible liquid start to deform when subjected to shear flow. If the conditions are met, the droplet may even breakup into daughter droplets. The study of a droplet in shear flow is important from the aspect of dispersion science and mixing process. For example, it is possible to create a specific blend morphology by shearing emulsions between two parallel plates with a small separation [1] which has applications in Lab-on-a-Chip devices [2]. This area is not only limited to laminar flows. According to Komrakova et al. [3], even though the flow regime in stirred tank reactors is fully turbulent, the effect of the existing eddies on droplets could be modeled by a laminar shear flow. Study of shear deformation of droplets can provide crucial understanding in morphology development of the blends, immiscible fluid displacement in enhanced oil recovery, refinement of liquids, carbon-dioxide sequestration, remediation of nonaqueous-phase liquids and emulsification.

Emulsification has wast applications in food, chemical, and pharmaceutical industries. Emulsification process takes place by applying shear stress against the surface tension, to elongate and then rupture a larger droplet into smaller ones. Emulsions can be made in many ways, however, shear mixing is one of the main methods. Thus Studies of shear deformation of droplets can be beneficial to better understand the properties of emulsions and to provides a deeper insight of rheological properties of the mixture. For instance, the critical conditions at which a droplet breaks-up is useful to quantify emulsion stability [4, 5].

Another one of important applications of deformation and breakup of confined sheared droplets is on Droplet-based microfluidic technology which has recently been exploited to perform microfluidic functions. Its applications range from fast analytical systems and synthesis of advanced materials [6] to protein crystallization [7] and biological assays for living cells [8, 9, 10] . Precise control of droplet volumes and reliable manipulation of individual confined droplets have crucial effects on the performance of these systems and are still a challenge [11]. Another important aspect of this area of study is in reacting dispersions, where an understanding of the dynamics of the droplet is needed in order to gain a better perception on the mechanisms of molecular transport, rates of chemical reaction and polymerization of the dispersion [12].

Since the experimental researches of Taylor [13, 14], droplet deformation and breakup in shear flow evoked great interests. More details on these studies could be found in reviews done by Rallison [15], Stone [16], Cristini and Renardy [17].

In the case where the droplet evolves to a steady shape, different parameters have been used by researchers to measure the deformation attained by the droplet. The first one is the Taylor deformation parameter

jesus@cttc.upc.edu (Jesús Castro), oliva@cttc.upc.edu (Assensi Oliva)

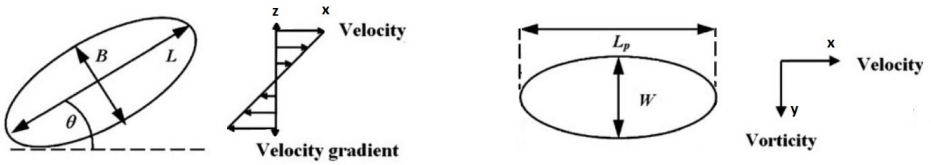

Figure 1: Schematic presentation of a deformed droplet along with related geometrical measurements in left: velocity-velocity gradient plane and right: velocity-vorticity plane

defined as $D = (L - B)/(L + B)$, where L and B are length and breadth of the drop, as shown in figure 1. Another parameter is the angle θ of orientation of the droplet with respect to the axis of shear strain. In addition to these parameters, Lp and W, as projected length and width of the droplet are used in literature and depicted in figure 1. In another experimental research, Marks [18] studied a single droplet undergoing end pinching in a strong shear flow in a process named "elongative end pinching". This process is in opposition to "retractive end pinching" process studied by Bentley and Leal [19]. Vananroye et al. [20] reported that confinement has a substantial effect on the critical capillary number. More studies in highly confined systems were done by Sibillo et al. [21], where they found oscillatory behavior in droplet deformation in high but subcritical capillary numbers. They also found complex breakup modes for supercritical capillary numbers. In the context of this paper, subcritical, refers to conditions where the deformation of the droplet reaches steady-state without any breakup and supercritical refers to conditions where the deformation of the droplet leads to breakup.

Analytical studies in this field are limited. Shapira and Haber [22, 23] investigated the effect of two parallel walls on the motion of a nearly spherical droplet and the drag force acting on it. Roths et al. [24] reported that in two-dimensional cases with small capillary numbers, Taylor deformation parameter is a linear function of capillary number. van der Sman and van der Graaf [25] used a slope equal to $f(\lambda_\mu) = 1.4$ for this linear function where λ_μ is the viscosity ratio of droplet to matrix. In three-dimension however, Stone [16] used $f(\lambda_\mu) = (16+19\lambda_\mu/(16+16\lambda_\mu))$. Richardson [26] reported a trigonometric function between deformation (D) and orientation (θ) of the droplet as $D \sim \cos(2\theta)$. Toose et al. [27] found out that time evolution of droplet deformation in two-dimension elongational flow follows the Oldroyd approximation and reported D=f(λ_μ)Ca exp(-$\gamma t/\tau$) where $\tau = Ca(1 + \lambda_\mu)$ where γ is the shear rate and $Ca = \mu\gamma r/\sigma$ as the capillary number is a measure of the ratio between the viscous and interfacial tension stresses. In this formulation, μ is viscosity, r is radius of the droplet, and σ is the surface tension coefficient. In a more recent work, Minale [28] presented a phenomenological model for the effect of wall on deformation of an

ellipsoidal droplet.

Besides the experimental and analytical studies, there are plenty of numerical researches in this field using mainly three methods of boundary integral, lattice Boltzmann (LB) and volume-of-fluid (VOF). Kennedy et al. [12], Kwak and Pozrikidis [29] and Janssen and Anderson [30] studied the droplet deformations using boundary integral method. Since in simulations of merging and folding interfaces in the boundary integral method, the interface point should be reconstructed, significant logical programming techniques are required which increases the computational costs. The mathematical implication of this method is described in Pozrikidis [31].

Using lattice Boltzmann model (LBM), van der Sman and van der Graaf [25] investigated the numerical criteria for correct analysis of emulsions and used them to study the droplet deformation and breakup in two-dimensional cases. Xi and Duncan [32] applied the LBM in conjugation with the interface force model presented by Shan and Chen [33] to simulate three-dimensional droplet deformation in simple shear flow. Komrakova et al. [3] used free energy LBM to perform three-dimensional simulations of liquid droplet deformation in simple shear flow for a wide range of flow conditions.

Volume-of-fluid (VOF) and coupled VOF/Level-set methods were used by many researchers [34, 35, 36, 37, 17, 38] to investigate the droplet deformation and breakup in shear flow. Li et al. [34] presented results for different values of capillary numbers and reported that for supercritical cases, by increasing the capillary number, the number of daughter droplets increases. Renardy and Cristini [35] studied the effect of inertia on droplet breakup. They reported that inertia rotates the droplet toward the vertical direction, in a mechanism similar to aerodynamic lift, afterward the droplet experiences higher shear, which pulls the droplet apart horizontally. Renardy et al. [36] fixed the flow's strength and focused on trends for the droplet fragment distribution when the size of the droplet increases. Khismatullin et al. [37] found that for viscosity ratios greater than the critical value, inertia can be used as a mechanism of breakup. Cristini and Renardy [17] worked on the effect of inertia and scaling fragments after droplet breaks.

The studies on shear deformation of the droplets is not limited to Newtonian fluids. Verhulst et al. [39] studied the influence of matrix and droplet viscoelasticity on the steady-state shear deformation of a droplet. Mukherjee and Sarkar [40] numerically investigate the effects of viscosity ratio on an Oldroyd-B droplet deforming in a Newtonian fluid under steady shear. They reported that the viscoelastic normal stresses reduce droplet deformation and increase critical capillary number. Hsu and Leal [41] studied the steady and transient deformations of a purely elastic droplet in a Newtonian fluid undergoing a planar extensional flow. They reported the absence of overshoot of the droplet deformation upon startup, and a

relative insensitivity to the Deborah number. Ioannou et al. [42] investigated the droplet deformation and breakup under simple shear flow when droplet and/or matrix represents non-Newtonian shear-thinning or shear-thickening behaviors. They stated that the shear-thinning droplets behave similarly to highly-viscous Newtonian droplets.

In this paper, we focus on three-dimensional simulations of droplet deformation and breakup in simple shear flow in the context of conservative level-set (CLS) method [43, 44, 45] with a finite-volume approach. In the present CLS method, interface normals are computed using a least-squares method on a wide and symmetric nodes-stencil around the vertexes of the current cell [44]. These normals are then used for an accurate computation of surface tension, without additional reconstruction of the distance function, as in geometrical volume-of-fluid/level-set methods [38] or fast-marching methods. Moreover, most of the computational operations are local, which permit an efficient implementation on parallel platforms [46]. The CLS method has been designed for general unstructured meshes [44]. Indeed, the grid can be adapted to any domain, enabling for an efficient mesh distribution in regions where interface resolution has to be maximized, which is difficult by using structured grids. Furthermore, TVD flux-limiter schemes [44] are used to discretize convective terms, avoiding numerical oscillations around discontinuities, whereas the numerical diffusion is minimized. Finally, the present finite-volume formulation is attractive due to the satisfaction of the integral forms of the conservation laws over the entire domain [45].

The first objective is to study the accuracy of our results on capturing the droplet's deformation and breakup in shear flow. The effect of domain size, mesh size and numerical parameters on the accuracy of the results are studied. Validation is done by analyzing the effect of different parameters including walls confinement, capillary number and viscosity ratio on the deformation and breakup of the droplet. The extracted results are compared with the available numerical, analytical and experimental data.

In the next step, the effect of viscosity ratio on walls critical confinement ratio for a constant capillary number of 0.3 and a low Reynolds number of 1.0 is studied. The walls critical confinement ratio divides the parameter space into the regions where droplets break or attain a steady shape. According to Vananroye et al. [47], for viscosity ratios smaller than 1, confinement suppresses breakup while for viscosity ratios bigger than 1, breakup is enhanced. Janssen et al. [48] further studied the deformation of a single droplet as a function of viscosity ratio and confinement ratio both experimentally and numerically using the boundary integral method. They discussed the critical capillary number for a wide range of viscosity ratios in different confinements and suggested that there is a generalized behavior on droplet breakup mechanism in confinement. They presented a graph of five regions for the critical capillary number in different confinements.

Despite these studies, to the best of our knowledge, effect of viscosity ratio on walls critical confinement ratio is yet to be discovered. In the last section of this paper, we elaborately study this phenomenon for a given capillary number of 0.3 and a low Reynolds number of 1.0. Our results illustrate two steady-state and one breakup regions for droplet under different confinements and viscosity ratios.

The outline of this paper is as follow: Mathematical formulations are presented in section 2. Employed numerical methods are explained in section 3. Section 4 involves the obtained results. Firstly we verify the accuracy of the method against different numerical, analytical and experimental data. In section 4.6, we study the effect of viscosity ratio on walls critical confinement ratio. Finally, concluding remarks are presented in section 5.

2. Mathematical formulation

Navier-Stokes equations are used to describe the conservation of mass and momentum of two incompressible immiscible newtonian fluids on a spacial domain Ω with boundary $\partial\Omega$ as following [44, 45]:

$$\frac{\partial}{\partial t}(\rho\mathbf{v}) + \nabla.(\rho\mathbf{v}\mathbf{v}) = -\nabla p + \nabla.\mu\left(\nabla\mathbf{v} + (\nabla\mathbf{v})^T\right) + \rho\mathbf{g} + \sigma\kappa\mathbf{n}\delta_\Gamma \text{ in } \Omega \quad (1)$$

$$\nabla.\mathbf{v} = 0 \text{ in } \Omega \quad (2)$$

where ρ and μ are density and dynamic viscosity of the fluids, $\mathbf{v}$ is the velocity field, p pressure field, $\mathbf{g}$ gravitational acceleration, and δ_Γ is the Dirac delta function concentrated at the interface (Γ). In this formulation, $\mathbf{n}$ is the unit normal vector outward to interface and κ is the interface curvature and σ is the interface tension coefficient.

Since the mass, density, and viscosity are constant within each fluid, they can be defined as scalar-fields inside the whole domain as follows:

$$\rho = \rho_1 H + \rho_2(1 - H) \quad (3)$$

$$\mu = \mu_1 H + \mu_2(1 - H) \quad (4)$$

where H is the Heaviside step function which takes the value one in dispersed phase and zero elsewhere.

In this research, conservative level-set (CLS) method [49], as introduced by Balcázar et al. [44] in the context of a finite-volume method for unstructured grid is used. Instead of the signed distance function, d(x,t), used to represent the interface in the classical level-set method, conservative LS method employs a

regularized indicator function ϕ as below:

$$\phi(x,t) = \frac{1}{2}\left(tanh\left(\frac{d(x,t)}{2\varepsilon}\right) + 1\right) \tag{5}$$

where ε is the parameter that sets the thickness of the interface. ϕ varies from 0 in one fluid to 1 in other fluid. With this formulation, interface is defined by $\Gamma = \{x|\phi(x,t) = 0.5\}$. Normal vector $\mathbf{n}$ on the interface and curvature κ of the interface, are obtained using [44]:

$$\mathbf{n} = \frac{\nabla\phi}{||\nabla\phi||} \tag{6}$$

$$\kappa(\phi) = -\nabla.\mathbf{n} \tag{7}$$

Note that based on the definition of regularized indicator function (ϕ) in the domain (value 1 in the dispersed phase and 0 in continuum phase, or vice-versa), the direction of $\mathbf{n}$ could be understood.

The level-set function is advected by velocity vector field, $\mathbf{v}$, provided from solution of Navier-Stokes equations. Since the velocity field is solenoidal ($\nabla.\mathbf{v} = 0$), the interface transport equation can be written in conservative form [44, 49]:

$$\frac{\partial\phi}{\partial t} + \nabla.\phi\mathbf{v} = 0 \tag{8}$$

Since sharp changes exist in level set function at the interface, Superbee flux limiter scheme is used in discretization of the convective term in order to minimize numerical diffusion and to avoid numerical instabilities at the interface. To keep the profile and thickness of the interface constant, an additional re-initialization equation [50] is used:

$$\frac{\partial\phi}{\partial\tau} + \nabla.\phi\left(1-\phi\right)\mathbf{n}_{\tau=0} = \nabla.\varepsilon\nabla\phi \tag{9}$$

where $\mathbf{n}_{\tau=0}$ is the interface normal vectors computed at the pseudo-time $\tau = 0$. This equation is advanced in pseudo-time τ and consists of a compressive flux: $\phi(1-\phi)\mathbf{n}_{\tau=0}$ and a diffusion term: $\nabla.\varepsilon\nabla\phi$. The first one keeps the level-set function compressed onto the interface along the normal vector $\mathbf{n}$, and the second one keeps the profile in prescribed characteristic thickness of ε. This parameter is defined based on the mesh

resolution as [44]:

$$\varepsilon_p = C_\varepsilon h^{1-\alpha} \tag{10}$$

where $h = (V_P)^{1/3}$ is the grid size based on volume V_P of cell P. In all the simulations of this paper, C_ε is constant and equal to 0.5. Parameter α, however, varies in order to change the thickness of the interface and can take values between [0,0.1], to overcome the possible numerical instabilities. The continuous surface force model (CSF) [51] is used for surface tension computation which converts the term $\sigma\kappa\mathbf{n}\delta_\Gamma$ in Eq. 1 to a volume force term as follows [44]:

$$\sigma\kappa\mathbf{n}\delta_\Gamma = \sigma\kappa(\phi)\nabla\phi \tag{11}$$

where $\nabla\phi$ is computed using least-square method based on vertex node stencils [44]. By applying this approach, the explicit tracking of the interface is not necessary.

3. Numerical method

Finite-volume (FV) approach is used to discretize the Navier-Stokes and level-set equations on a collocated grid, so all the computed variables are stored at centroids of the cells [44]. A central difference (CD) scheme is used to discretize the compressive term of re-initialization equation (9) and diffusive fluxes at the faces. A distance-weighted linear interpolation is used to calculate the face values of physical properties and interface normals. The gradients are computed at the cell centroids using the least-squares method. For creeping flow regime, a central difference scheme and for non-creeping flow regimes a total-variation Diminishing (TVD) SUPERBEE flux limiter is used to discretize the convective term as implemented in Balcázar et al. [44], in order to improve the numerical stability of the solver. At discretized level, physical properties are regularized in the context of the CLS method. Therefore a linear average is used for density as $\rho = \rho_1\phi + \rho_2(1-\phi)$, and a harmonic average is used for viscosity as $\mu = \left(\frac{\phi}{\mu_1} + \frac{1-\phi}{\mu_2}\right)^{-1}$. Harmonic average of viscosity improves the accuracy convergence of the results, compared with the linear average. As a comparison, velocity profile of a two-dimensional two-phase oscillating droplet is presented in appendix Appendix B where results of harmonic averages of viscosity are compared with results of linear average of viscosity for this problem.

A classical fractional step projection method as described by Chorin [52] is used to solve the velocity-pressure coupling. The solution procedure in each timestep is as follows:

1. Physical properties, interface geometric properties and velocity field are initialized.

2. Allowable time step is calculated. The value of Δt is limited by CFL conditions on convective term and also by explicit treatment of surface tension as used by [44, 45]:

$$\Delta t_{conv} \equiv \alpha \times min(\frac{h}{\|V_P\|}) \tag{12}$$

$$\Delta t_{cap} \equiv \alpha \times min(h^{3/2}(\frac{\rho_1 + \rho_2}{4\pi\sigma})^{1/2}) \tag{13}$$

   where α is CFL coefficient. The final global value of time step is the minimum of Δt_{conv} and Δt_{cap}. To decrease the computational costs, the maximum value of α which leads to a stable simulation is used. Unless otherwise mentions, this value is 0.1.

3. The advection equation (8) is integrated in time with a 3-step third order accurate TVD Runge-Kutta scheme [53].

4. The re-initialization equation (9) is integrated in pseudo time (τ) using a third order accurate TVD Runge-Kutta scheme. The time τ is used to lead the solution into a stationary state. Since an explicit scheme is used, the time step is restricted by the viscous term of equation 9 as follows [44, 49]:

$$\Delta\tau = C_\tau min\left(\frac{h^2}{\varepsilon_P}\right) \tag{14}$$

   One iteration is used to solve the discretized form of equation 9. The value of C_τ in this formula serving as a CFL-like coefficient for this equation, can take values between [0.01,0.05].

5. Physical properties in the domain (density and viscosity) and geometrical properties at the interface (curvature and interface normal) are updated from the level set field.

6. The velocity and pressure fields are calculated using a fractional-step method. The first step is to calculate the predicted velocity $\mathbf{v}$. In the creeping flow regime, where the Reynolds number of the flow is close to zero, the diffusion term in momentum equation tends to control and decreases the time step. This implies a huge computational cost on simulations. To avoid this issue, diffusion term could be treated implicitly. So a second-order implicit Crank-Nicolson scheme is used to discretize the diffusion term of equation 1 while a second-order Adams-Bashforth scheme is used on convective, gravity and surface tension terms.

$$\frac{\rho \mathbf{v}^* - \rho^n \mathbf{v}^n}{\Delta t} = \frac{3}{2}(R_h^v)^n - \frac{1}{2}(R_h^v)^{n-1} + \frac{1}{2}\left(\mathbf{D}_h(\mathbf{v}^*) + \mathbf{D}_h(\mathbf{v}^n)\right) - \nabla_h p^n \tag{15}$$

where $R_h^v = -\mathbf{C}_h(\rho \mathbf{v}) + \rho \mathbf{g} + \sigma \kappa \nabla_h(\phi)$ with $\mathbf{C}_h(\rho \mathbf{v}) = \nabla_h.(\rho \mathbf{v}\mathbf{v})$ as the convective operator. In this equation, $\mathbf{D}_h(\mathbf{v}) = \nabla_h.\mu(\nabla_h \mathbf{v} + \nabla_h^T \mathbf{v})$ as the diffusion operator where ∇_h represent the gradient operator.

A term of pressure gradient of previous time step is added to the discretized form of equation 1. According to Armfield and Street [54], this will increase the accuracy of the momentum equation to a second order in time, and combined with proper boundary condition of Kim and Moin [55] even to a third order in time. In our case, the momentum equation has a second-order accuracy in time. In appendix Appendix C, the convergence of implemented method for the accuracy of momentum equation in time is analyzed.

Next, a correction to the predicted velocity applies as:

$$\frac{\rho \mathbf{v}^{n+1} - \rho \mathbf{v}^*}{\Delta t} = -\nabla_h \pi^{n+1} \tag{16}$$

where π is the pressure correction term. By applying the incompressibility constraint ($\nabla.\mathbf{v} = 0$), equation 16 changes to a Poisson equation as follows:

$$\nabla_h.\left(\frac{1}{\rho}\nabla_h(\pi^{n+1})\right) = \frac{1}{\Delta t}\nabla_h.(\mathbf{v}^*) \tag{17}$$

The obtained linear system is solved using a preconditioned conjugated gradient method. At the end, the velocity $\mathbf{v}^{n+1}$ is corrected using:

$$\mathbf{v}^{n+1} = \mathbf{v}^* - \frac{\Delta t}{\rho}\nabla_h(\pi^{n+1}) \tag{18}$$

and the pressure is updated using:

$$\mathbf{p}^{n+1} = \mathbf{p}^n + \pi^{n+1} \tag{19}$$

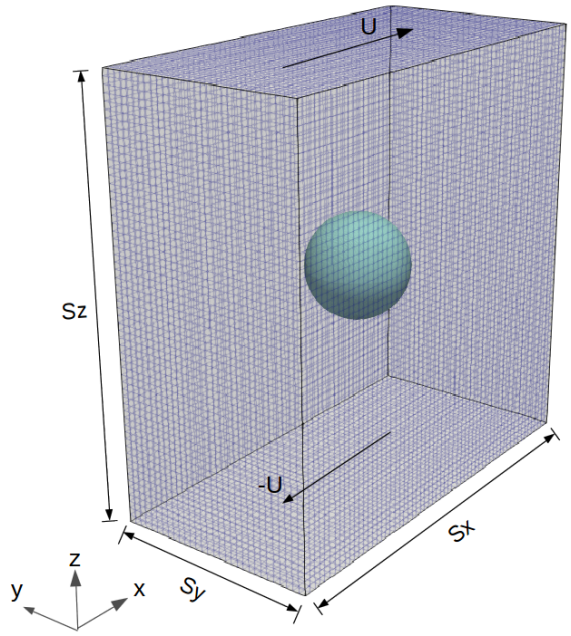

Figure 2: Computational setup in the cubic structured mesh

7. In order to fulfill the incompressible constraint, Eq. 2, and to avoid pressure-velocity decoupling on collocated meshes [56, 57], a cell-face velocity is used to advect the momentum and CLS function, as introduced in [44, 58].

8. repeat steps 2 -7 to reach the desired time.

The reader is referred to [58, 44] for technical details on the finite-volume discretization of both the Navier-Stokes and conservative level-set equations on collocated unstructured grids. The numerical methods are implemented in an in-house parallel c++/MPI code called TermoFluids [59]. Validations and verifications of the numerical methods in the context of Conservative level-set method used in this work have been reported in [44, 43, 50, 38, 45, 46, 58, 60, 61].

4. Numerical experiments and discussion

A circular droplet with radius r is placed at the center of a domain with span S_x, S_y and S_z in x,y and z directions, respectively. Figure 2 illustrates the initial computational setup. The opposite x-direction velocities of $+U$ and $-U$ are imposed at the top and bottom walls inducing a shear rate of $\dot{\gamma} = 2U/S_z$ in the domain. A periodic boundary condition is applied in the flow direction (x) and Neumann boundary condition in y direction. Computations have been performed using a Cartesian mesh of cubic grids with the

edge size of h. This mesh was generated by a constant step extrusion of the two-dimensional y-z grid along the x-axis with the step size of h. At the beginning of the simulation, a linear velocity field is applied inside of the domain varying from $-U$ at the bottom wall to $+U$ at the top wall. Simulations with different mesh resolutions are done to study the effect of the computational grid size.

The system can be physically defined by four parameters of Reynolds number (Re), capillary number (Ca), viscosity ratio ($\lambda = \mu_d/\mu_c$) and walls confinement ratio ($2r/S_z$) while c stands for *continuum* and d stands for *droplet*. For an arbitrary value of shear rate ($\dot{\gamma}$), the velocity at the top and bottom walls are calculated as $U = \dot{\gamma} S_z/2$. Then viscosity is calculated using the Reynolds number as below:

$$Re = \frac{\rho_c \dot{\gamma} r^2}{\mu_c} \tag{20}$$

The capillary number is a dimensionless parameter defining the relative effect of the shear stress versus surface tension across the interface, given by:

$$Ca = \frac{\dot{\gamma} \mu_c r}{\sigma} \tag{21}$$

For a given value of Ca and Re numbers, and the calculated value of μ_c, the related value of σ is determined.

The effect of variable CLS parameters of C_τ and α on the results is studied in Appendix A. According to this study, the variation of C_τ and α has negligible effect on the deformation of the droplet, and thus constant values of 0.015 and 0.0 are choosen for these two parameters, respectively. In Appendix A, we have also shown that our numerical tools conserve the mass of the droplet perfectly.

4.1. The effect of domain length

In order to study the effect of domain's length on the results, simulations with $(Re, Ca, \lambda) = (0.1, 0.3, 1)$ in three domains with $(S_x, S_y, S_z) = (6r, 4r, 8r)$, $(8r, 4r, 8r)$ and $(10r, 4r, 8r)$ with grid size of $h = 2r/25$ are performed. The value of D and θ parameters for these cases are tabulated in table 1.

It is plain to see that domains with lower lengths encounter with a lower value of D and higher inclination angle. Since periodic boundary condition is applied in the flow direction, it is important to make sure that the fluctuations in the velocity profile downwind of the domain will dissipate before passing through the periodic boundary and re-entering the domain. The ideal velocity profile at this location should linearly

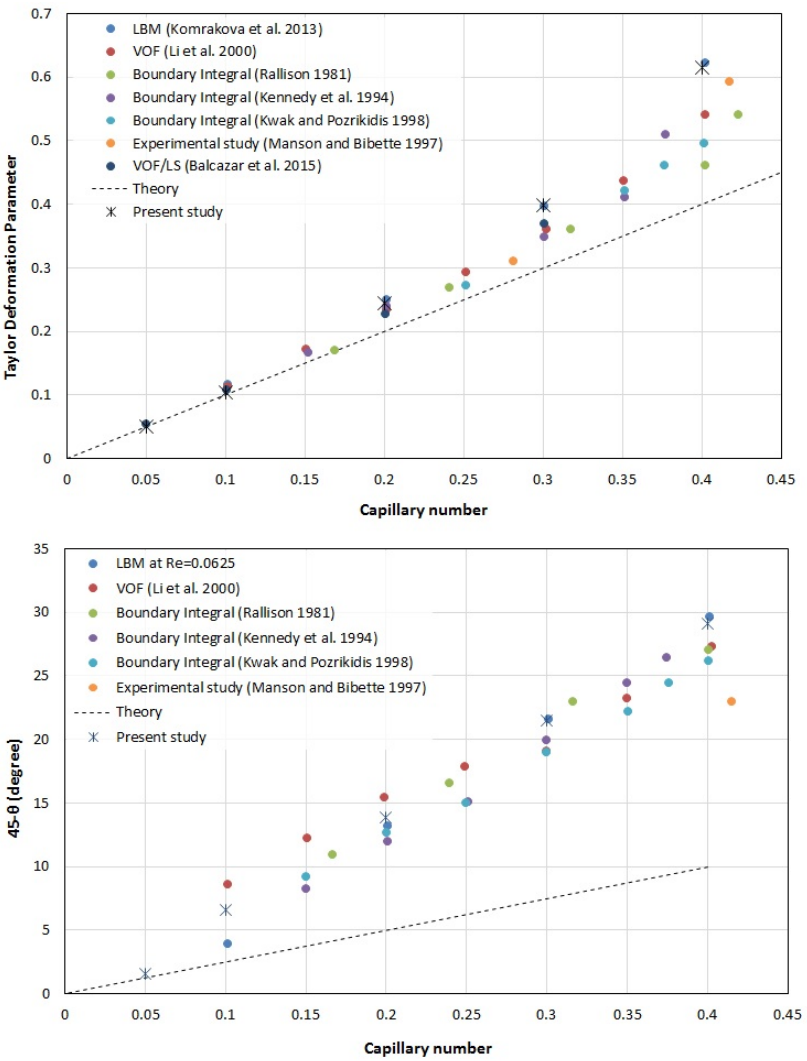

Figure 3: Taylor deformation parameter (D) and inclination of the droplet (45-θ) at steady-states for different capillary numbers, in Stokes flow conditions (Re=0.0625) with $\lambda = 1$. Dash line represents the asymptotic results by Cox [62] for small deformation.

Table 1: The effect of domain's length (S_x) on steady-state values of Taylor deformation parameter (D) and orientation angle (θ) for cases with $Re = 0.1, Ca = 0.3$ and $\lambda = 1$. The S_z and S_y of the domains are 8r and 4r, respectively.

S_x	$6r$	$8r$	$10r$
D	0.3823	0.3985	0.4039
θ	25.15	24.50	24.34

Table 2: The effect of grid size on Taylor deformation parameter (D) at steady-state for cases with Re=0.1, $\lambda = 1$ and two different capillary numbers of 0.1, 0.4.

mesh	h	Ca=0.1		Ca=0.4	
		D	ε_D	D	ε_D
M1	2r/25	0.1139	1.24%	0.6313	4.7%
M2	2r/30	0.1135	0.8%	0.6144	1.9%
M3	2r/35	0.1125	-	0.6030	-

vary from -U at the bottom wall to +U at the top wall. According to measurements and extracted profiles, domain with $S_x = 6r$ has nonuniform velocity profile at the location of the periodic boundary. This issue affects the deformation of the droplet, while domain with $S_x = 10r$ has a much more uniform velocity distribution at this location. The standard deviation of D for cases with $S_x = 6r$ and $S_x = 8r$ is 1.1% while this value for cases with $S_x = 8r$ and $S_x = 10r$ is 0.3%. In order to reduce the computational cost, unless otherwise is mentioned, the length of the domains of simulations is $S_x = 8r$. According to our studies and Komrakova et al. [3], $S_y = 4r$ is wide enough to minimize the effect of the side walls on simulations and save-up in computational costs. Hence, unless otherwise is mentioned, domains with $S_y = 4r$ are used in the simulations.

4.2. Grid convergence analysis

Concerning with the effect of grid size on results, simulations with Re=0.1, λ=1 and two different capillary numbers of 0.1 and 0.4, as the boundaries of the subcritical regime of creeping flow, are done. Table 2 summarizes the Taylor deformation parameter for these cases solved in three different meshes of M1, M2, and M3. The mesh M3 (as it is formed with the finest grid) is used as the reference case, and the relative error of cases with meshes M1 and M2 with regards to the case with this mesh are calculated. According to these data, the error in Taylor deformation parameter of mesh M2 in the worse case is less than 2%. In favor of computational cost, unless otherwise is specified, simulations are done in domains with grid size of mesh M2.

4.3. The effect of capillary number

In order to study the accuracy of our results on capturing the effect of capillary number on deformation of the droplet in creeping flow condition, simulations with different capillary numbers of 0.05, 0.1, 0.2, 0.3 and 0.4 in flow with Re=0.0625 and $\lambda = 1$ are done. For the case with Ca=0.4, a domain length of $S_x = 12r$ is used to ensure acceptable uniform velocity profile at the location of the periodic boundary.

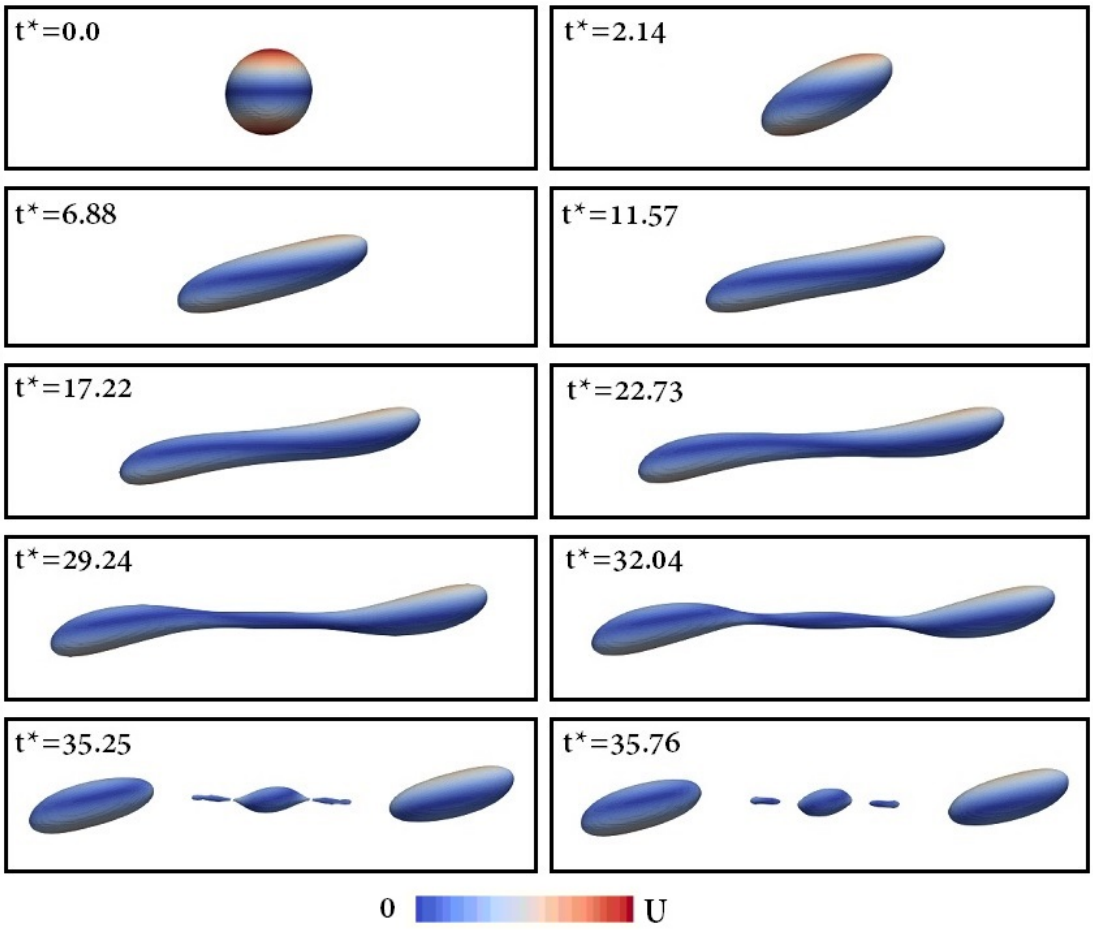

Figure 4: Evolution of droplet shape at Re=0.1, Ca=0.42 and λ=1, along with the velocity magnitude contours on the droplet surface, ($t^* = t\dot{\gamma}$).

Taylor deformation parameter (D) and inclination of the droplet (45-θ) are extracted and presented in figure 3. These data are compared with results available in the literature, done by different methods i.e. numerical methods including Lattice Boltzmann, VOF and boundary integral in addition to experimental and analytical methods. The results extracted in this study agree well with the reference data.

For aforementioned cases, with capillary numbers of 0.2, 0.3 and 0.4, the steady-state droplet shape and evolution of droplet deformation are illustrated in supplementary material figure 1 and 2.

According to the previous experimental, numerical and theoretical studies, in creeping flow conditions, when $\lambda < 4$, there is a critical capillary number (Ca_c) above which the droplet won't reach steady-state and continues to deform until breaks-up. The value of Ca_c is lowest for λ values roughly around 0.6 [63]. According to Rallison [15], this value is slightly less than Ca_c for $\lambda = 1$ which is around 0.41. As reported

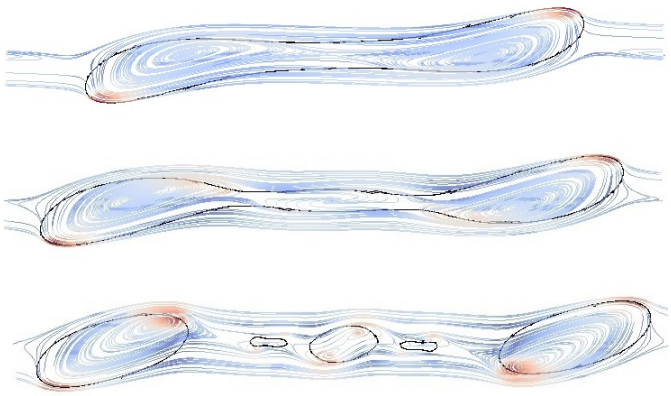

Figure 5: Evolution of the droplet shape and the flow pattern inside of the droplet, along with the vorticity magnitude contours all at $y = S_y/2$, for the case with Re=0.1, Ca=0.42 and λ=1. Snapshots are taken in times $t\dot{\gamma} = 25.20, 32.04$ and 35.76 (from top to bottom).

by Li et al. [34], in case of Ca=0.42, the droplet breaks into two daughter droplets, one satellite, and two sub-satellite droplets. In order to study the ability of the method on capturing the breakup, simulation with Ca=0.42, Re=0.1 and $\lambda = 1$ in a domain with $(S_x, S_y, S_z) = (12r, 4r, 8r)$ is carried out. The droplet shape evolution is presented in figure 4. As expected, the droplet breaks-up into two daughters, one satellite in the middle and two sub-satellite droplets. In order to gain a better understanding of the breakup process, the final stages of the breakup of this case are illustrated in figure 5. This figure presents the cross-sectional profile of the surface of the droplet ($\phi = 0.5$) at three different times of $t\dot{\gamma}$=25.20, 32.04 and 35.76 along with the velocity streamlines and vorticity magnitude contours. According to this figure, at time $t\dot{\gamma}$=25.20, there are two visible vortices inside of the droplet elongated in the flow direction, each in one of the bulbous. As time passes to $t\dot{\gamma}$=32.04 and droplet evolves, a third vortex is formed inside of the waist of the droplet which is separated from the other two vortices by the necks. Towards the end, where the waist breaks into a satellite and two sub-satellite droplets, the vortex inside of it also divides into three vortices, one inside of each piece.

4.4. The effect of walls confinement

In favor of studying the ability of the proposed method on capturing the effect of walls confinement on droplet deformation in subcritical regions, simulations with (Re, Ca, λ)=(0.1,0.3,1) and (0.1,0.1,1) are done in domains with different confinement ratios ($2r/S_z$). As reported by Renardy and Cristini [35], for the given Reynolds number of 0.1 and λ value of 1, capillary numbers of 0.1 and 0.3 are below the critical value (Ca_{cr}) which means the droplet must reach to a steady-state. Shapira and Haber [23] extracted the analytical

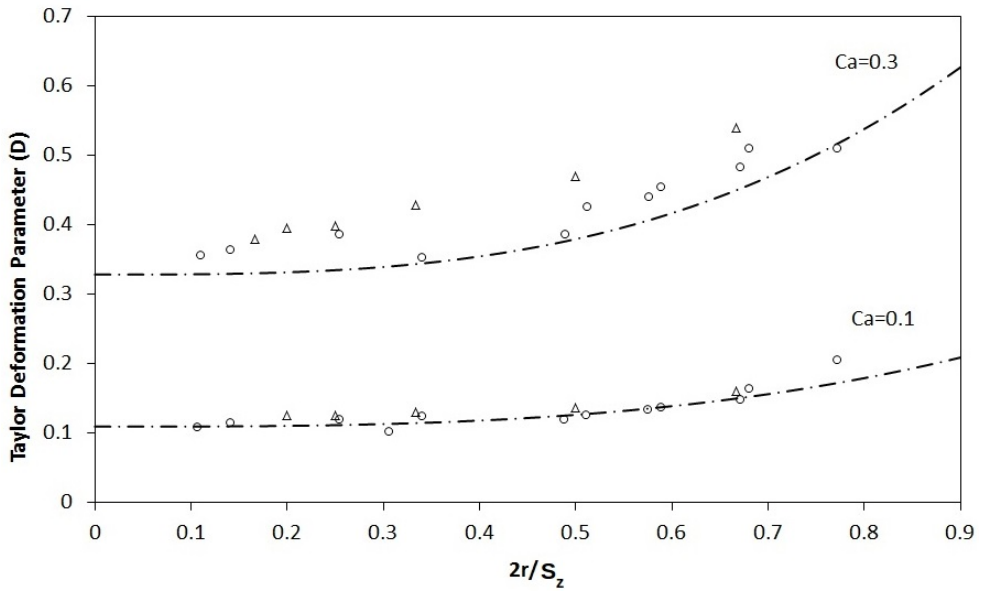

Figure 6: Taylor deformation parameter (D) for cases with Ca=0.1 and 0.3 with $\lambda = 1$ in different walls confinement ratios. Experimental data of Sibillo et al. [21] (○) and analytical data of Shapira and Haber [23] (dash dot lines) for Stokes flow regime, in comparison with results of current study for Re=0.1 (△)

expressions based on Lorentz's reflection method for droplet deformation in confined shear flow in small to moderate deformation regimes. They presented a first-order correction for the wall effect and claimed that the droplet shape was not altered compared to the unbounded shear flow but only the magnitude of deformation was increased.

The results of simulations of current study compared with the experimental data of Sibillo et al. [21] and analytical studies of Shapira and Haber [23] are presented in figure 6. As can be seen in this figure, for both capillary numbers, Taylor deformation parameter (D) increases with increasing the walls confinement ratio ($2r/S_z$). In smaller capillary number (Ca=0.1) there is good agreement between analytical predictions of Shapira and Haber [23] and both experimental data of Sibillo et al. [21] and the results of current study. For cases with Ca=0.3, however, analytical predictions of Shapira and Haber [23] fails to predict the Taylor deformation parameter compared with experimental data of Sibillo et al. [21] and results of the present study. For all the cases, by decreasing the walls confinement ratio, the value of Taylor deformation parameter converges to a constant value.

In the next step, we study the startup behavior of a highly confined droplet with $2r/S_z = 0.83$, Ca=0.6, λ=0.32 and Re=0.0625 in a domain with $S_x = 16r$. As stated in Vananroye et al. [47], the critical capillary

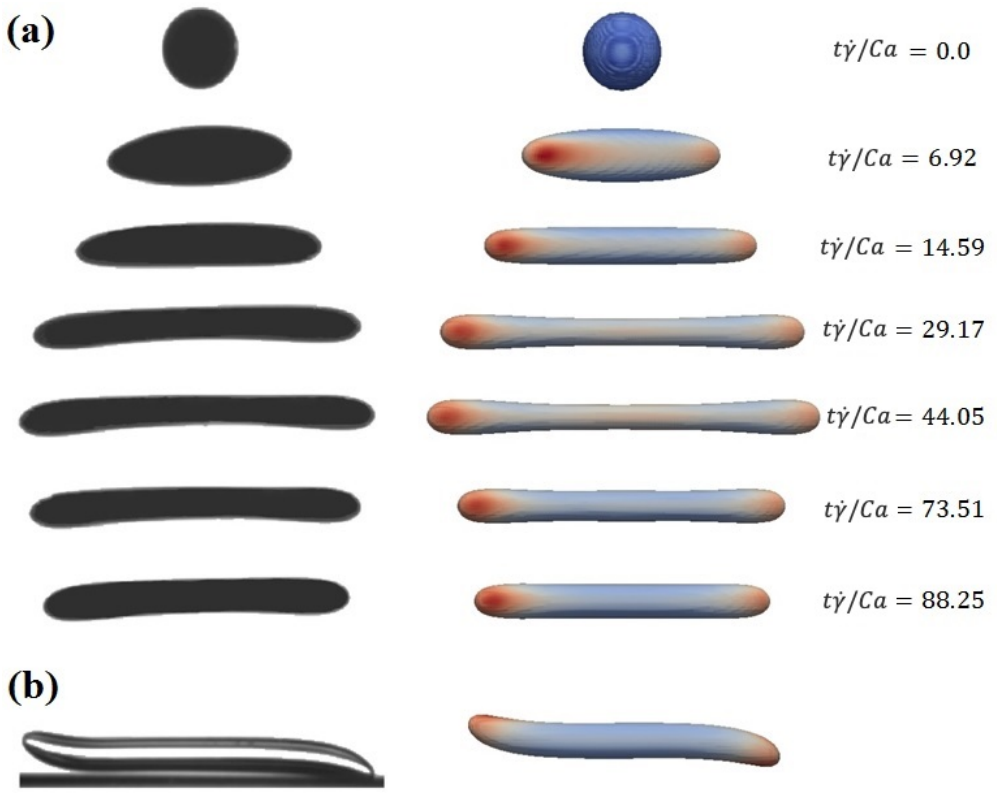

Figure 7: Time evolution of a highly confined droplet in creeping flow condition with $2r/S_z = 0.83$, $\lambda = 0.32$, and Ca=0.6, along with the pressure contours on the droplet's surface (right column) compared with experimental results of Vananroye et al. [64] (left column). (a): images taken in velocity-vorticity plane, (b): images taken in velocity-velocity gradient plane at $t\dot{\gamma}/Ca$=88.25

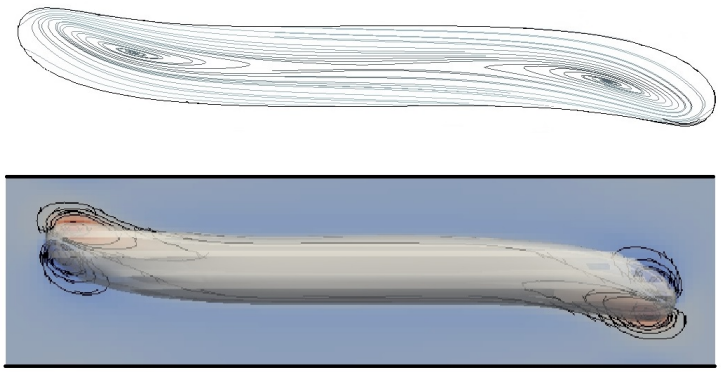

Figure 8: Top: Streamline contours inside of the droplet in x-z plane at $y = S_y/2$, Bottom: droplet shape along with the walls and vorticity contours ($e_y.\nabla \times \mathbf{v}$) in x-z plane at $y = S_y/2$. Both shapes illustrates a droplet in creeping flow conditions, with capillary number of 0.6, $\lambda = 0.32$, Reynolds number of 0.0625 and walls confinement ratio of $2r/S_z = 0.83$ at $t\dot{\gamma}/Ca$=88.25

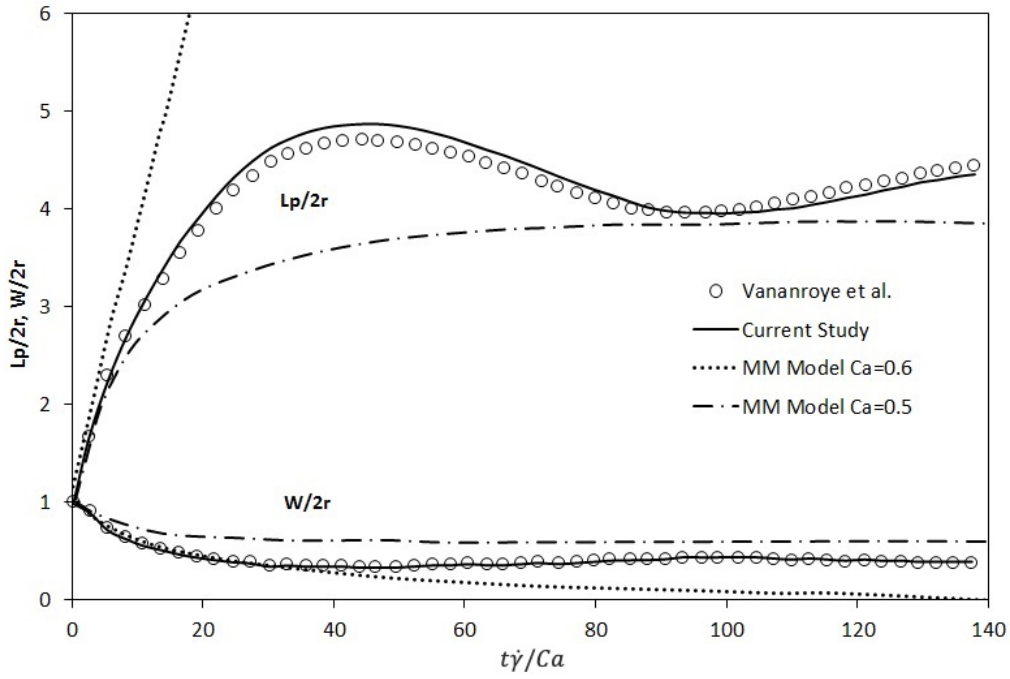

Figure 9: Startup behavior of a highly confined droplet with Re=0.0625, $2r/S_z = 0.83$, $\lambda = 0.32$, and Ca=0.6. compared with experimental results of Vananroye et al. [64] for creeping flow condition and confined MM model of Minale [28] for Ca=0.5, 0.6

number for a case with λ=0.32, $2r/S_z$=0.83 and creeping flow condition is approximately equal to (Ca_{cr} =)0.7. Thus for our intended case, we do not expect the breakup of the droplet. Figure 7 illustrates the time evolution of the droplet in comparison with the same time instants of the experimental work of Vananroye et al. [64].

According to the figure 7(a), shortly after starting the simulation, the droplet starts to stretch in the flow direction. The stretching continues until the droplet reaches its maximum elongation at some time around $t\dot{\gamma}/Ca$=44, but instead of breaking up, the droplet retracts. According to figure 7(b), the central part of the droplet takes a cylindrical shape, oriented in the flow direction and the tips are tilted towards the walls giving the droplet a sigmoid shape. Figure 8 provides information about the streamline contours inside of the droplet and vorticity contours in $y = S_y/2$ plane. According to this figure, two vortices exist inside of the droplet which are stretched from the center of the droplet toward the tips.

Time variation of W/2r and L_p/2r parameters, along with experimental data of Vananroye et al. [64] and analytical predictions of MM model Minale [28] are presented in figure 9. According to this figure, for the time around $t\dot{\gamma}/Ca$ ≈44, the value of L_p/2r is maximum which is in agreement with information provided in figure 9. Also for the time around $t\dot{\gamma}/Ca$ ≈95, the droplet starts to expand after reaching a local minimum length. It seems that these oscillations in the deformation of the droplet will last for a long time and reaching steady-state will take time much longer than the scale studied in this paper ($t\dot{\gamma}/Ca$ =140). It is worth mentioning that in this case a good agreement is seen between the experimental data and the results of current study. MM model of Minale [28] however fails to provide accurate information. In this model for Ca=0.6, the droplet continuously deforms until it breaks-up. For smaller capillary of 0.5, this model predicts a steady-state after $t\dot{\gamma}/Ca$ ≈80 and does not predict any oscillations in the droplet deformation.

4.5. The effect of viscosity ratio

In order to study the accuracy of the method on a wider range of viscosity ratios, three simulations with viscosity ratios of λ=0.28, 1.2 and 1.9 all with Ca=0.2 and Re=0.1 are performed. The selected domain has walls confinement ratio of $2r/S_z = 0.73$. Figure 10 presents the startup transition of non-dimensionalized L and B parameters along with the experimental results of Vananroye et al. [64] and predictions of confined MM model of Minale [28]. It is clear to see that the startup transition of the droplets in all three cases are similar, although approximately after $t\dot{\gamma}/Ca$ ≈3 the differences start. Good agreement is seen between experimental data and results extracted in this study. The MM model results also match the startup transition process predicted by experimental and numerical results. However, it over-predicts the deformation of the droplet for the rest of the simulations.

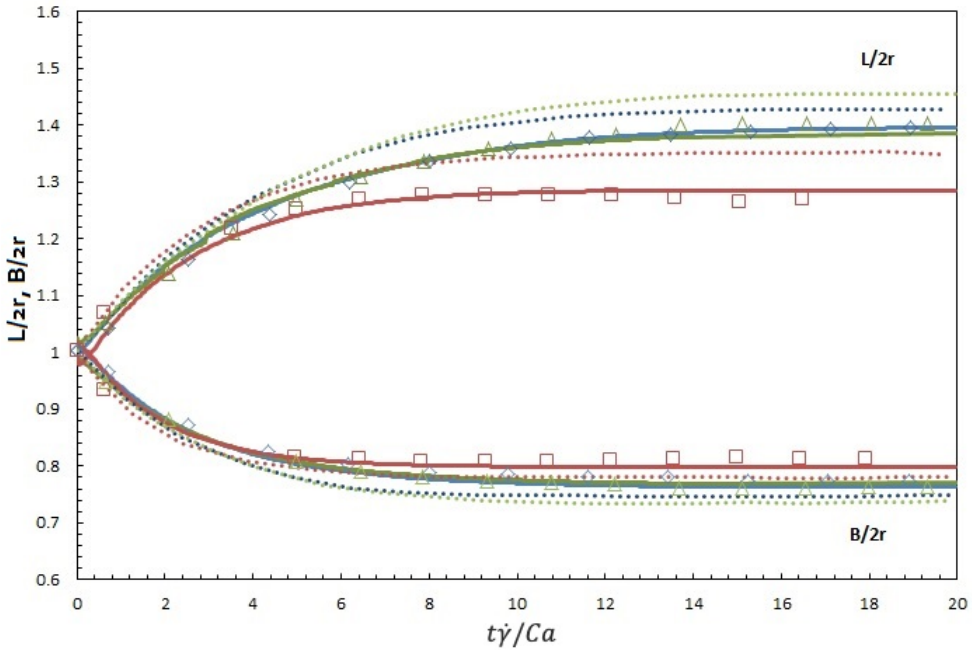

Figure 10: Effect of viscosity ratio on transition of droplet deformation for Ca=0.2 in a domain with confinement ratio of $2r/S_z = 0.73$. Comparison between extracted data from experimental results of Vananroye et al. [64] (symbols) and prediction of confined MM model of Minale [28] (dash lines) for creeping flow condition, along with the extracted results of current study (bold lines) for Re=0.1. Information in color red stand for $\lambda = 0.28$, color blue for $\lambda = 1.2$ and color green for $\lambda = 1.9$. The absolute time (t) is non-dimensionalized with characteristic emulsion time (τ).

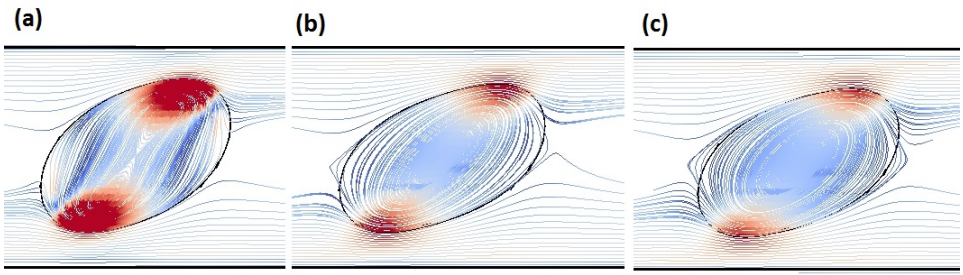

Figure 11: Cross sectional steady-state scheme of droplet in $y = S_y/2$, along with stream lines of the flow in different viscosity ratios of 0.28 (a), 1.2 (b) and 1.9 (c), for flow with Re=0.1 and Ca=0.2. All the simulations are done in a domain with $2r/S_z = 0.73$. The color contours presents the vorticity magnitude in aforementioned plane.

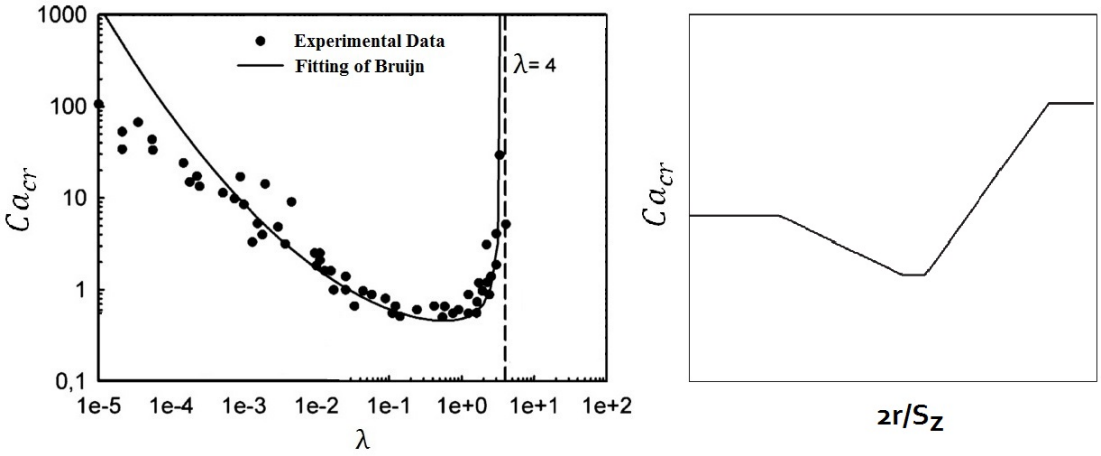

Figure 12: Left: Effect of viscosity ratio on droplet breakup in simple shear flow. Experimental data from [63], Right: Schematic representation of the effect of walls confinment ratio on critical capillary number as presented in Janssen et al. [48]

Figure 11 illustrates the cross-section of the droplet shape in x-z at $y = S_y/2$ plane at time $t\dot{\gamma}/Ca$ =20, along with the velocity streamlines and vorticity magnitude contours. According to this figure, for the case of $\lambda = 0.28$, there are two vortices inside of the droplet, but by increasing the viscosity ratio to 1.2 and 1.9, it decreases to one vortex. Also, the vorticity magnitude decreases by increasing the viscosity ratio. Since $\lambda = \mu_d/\mu_c$, smaller viscosity ratio means for a constant matrix viscosity, the droplet has lower viscosity, and hence lower resistance towards the gradual deformation. That justifies the bigger deformation in the flow pattern, two vortices and higher vorticity magnitude inside of the droplet with $\lambda = 0.28$.

4.6. The effect of viscosity ratio on walls critical confinement ratio

In previous sections, we validated the ability of our method on capturing the physics of problems with different walls confinements (section 4.4) and viscosity ratios (section 4.5). We realized that increasing the confinement ratio for subcritical cases increases the droplet deformation parameter (fig. 6) and for highly confined cases, induces retractions and expansions in the droplet which causes fluctuations in the deformation (fig. 9). We also noticed that by varying the viscosity ratio, the flow pattern inside of the droplet changes, as increasing the viscosity ratio from 0.28 to 1.2 decreased the number of internal vortices of the droplet from two to one, and also decreased the vorticity magnitude (fig. 11).

Grace [63] systematically studied the droplet breakup in simple shear flow as a function of viscosity ratio. These data are now known as Grace curve which is presented in figure 12 (left). In this figure, the values of λs which are above the fitted line prompt the breakup, while values of λ under it results in steady-state

Table 3: subcritical (sub) and supercritical (super) values of viscosity ratios for different walls confinement ratios along with the final values of D, θ, Lp/2r and W/2r for subcritical cases. l and h in λ stand for low and high as in each confinement ratio there are two values of λ_{cr}, one smaller than the other.

$2r/S_z$		λ_{sub}	λ_{super}	D	θ	Lp/2r	W/2r
0.25	λ_l	0.2	0.3	0.48	25.32	1.70	0.75
	λ_h	2.55	2.5	0.49	17.25	1.70	0.76
0.38	λ_l	0.35	0.4	0.53	21.64	1.82	0.74
	λ_h	2.2	2.0	0.49	17.52	1.79	0.75
0.50	λ_l	0.65	0.7	0.6	16.67	2.1	0.715
	λ_h	2.0	1.95	0.56	14.45	2.02	0.72
0.71	λ_l	1.4	1.5	0.7	11.16	2.47	0.6
	λ_h	5	4.5	0.56	11.03	2.0	0.69
0.83	λ_l	1.75	2.0	0.76	8.52	2.84	0.54
	λ_h	14	13	0.54	8.28	1.95	0.67

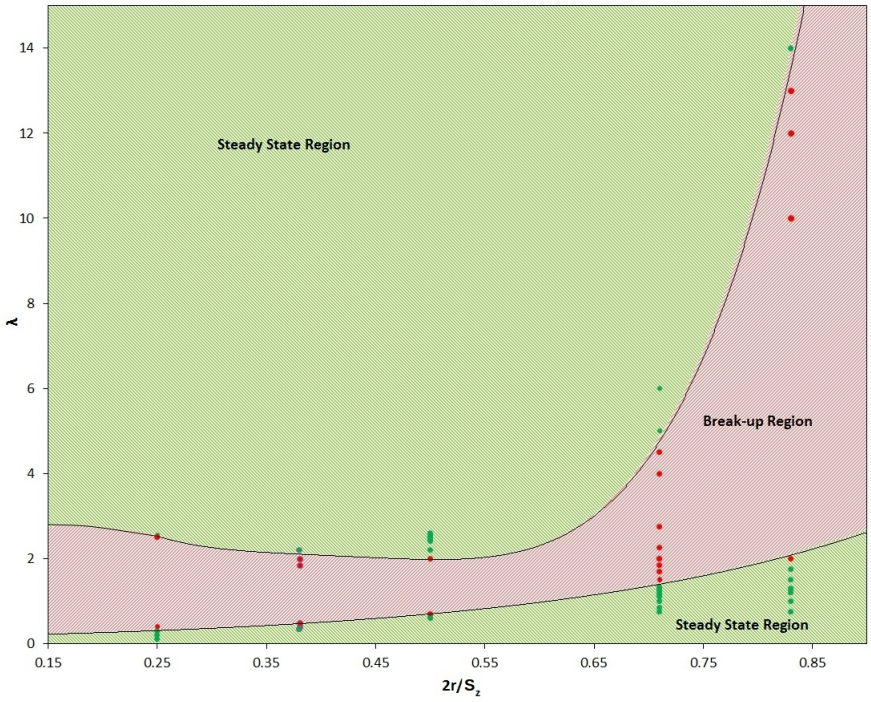

Figure 13: The effect of viscosity ratio on walls critical confinement ratio in steady-state deformation and breakup of the droplet, for given values of Ca=0.3 and Re=1.0 (The trend lines are added for the sake of clarity).

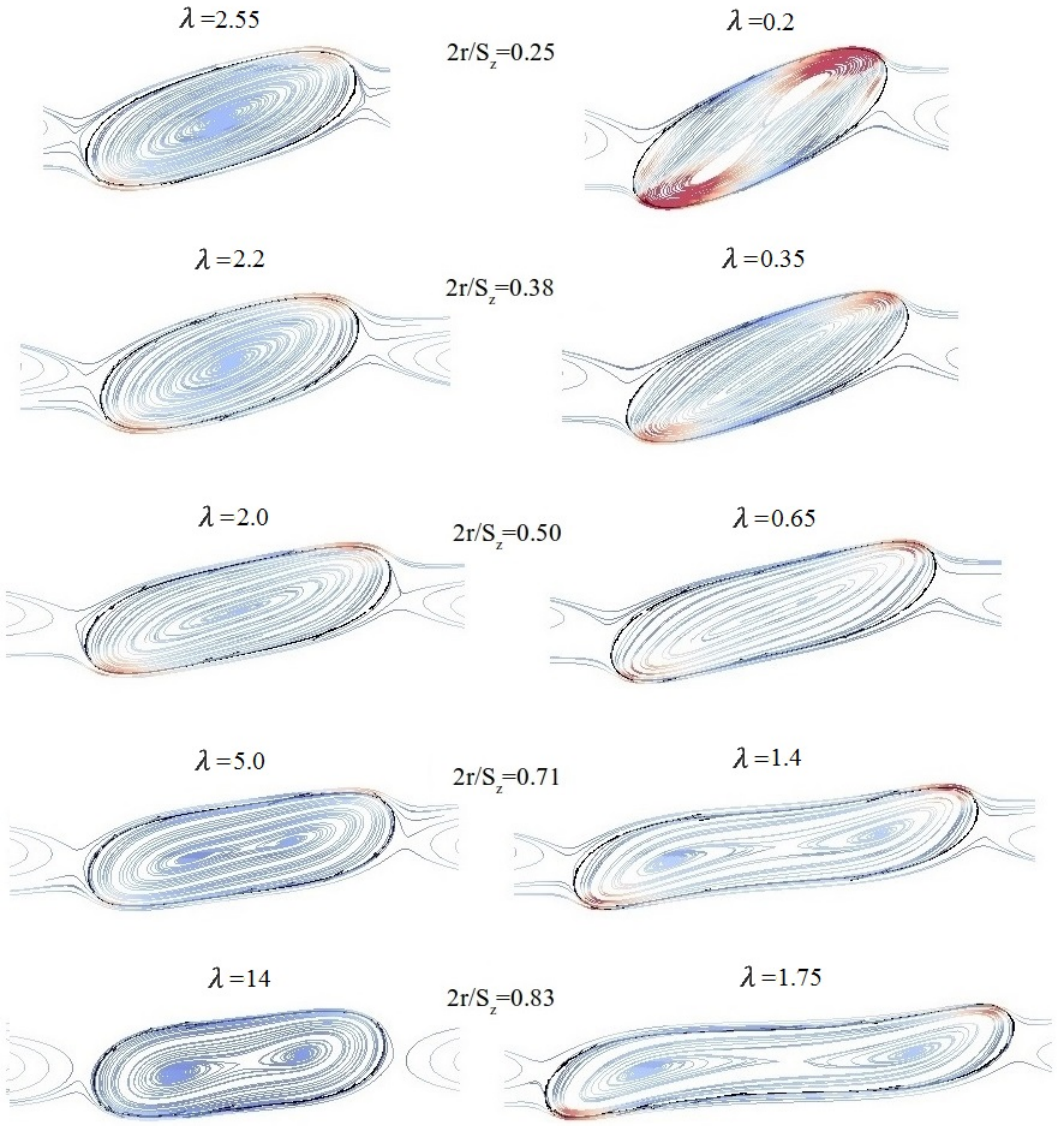

Figure 14: The steady-state droplet shape along with the streamlines of the flow inside of the droplet in $y = S_y/2$, for subcritical cases in higher steady-state region (left column), and subcritical cases in lower steady-state region (right column) in different confinement ratios. The color contours present the vorticity magnitude in the aforementioned plane.

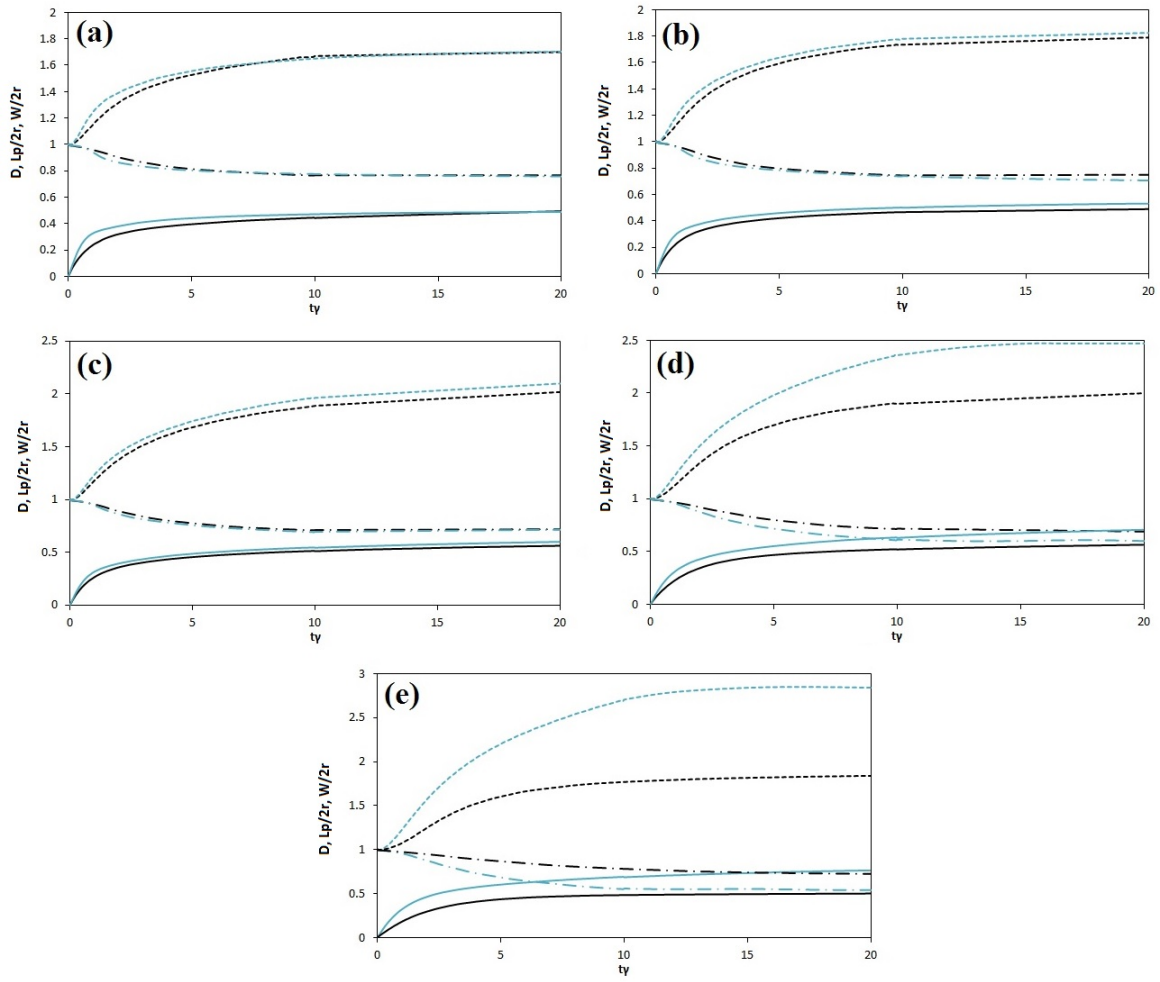

Figure 15: D (solid lines), $L_p/2r$ (dash lines) and W/2r (dash dot lines) parameters Vs. $t\dot{\gamma}$ for subcritical cases of table 3. Black color lines are related to the results of λ_h and green color lines are related to the results of λ_l. $2r/S_z=$ (a): 0.25, (b): 0.38, (c): 0.50, (d): 0.71 and (e): 0.83.

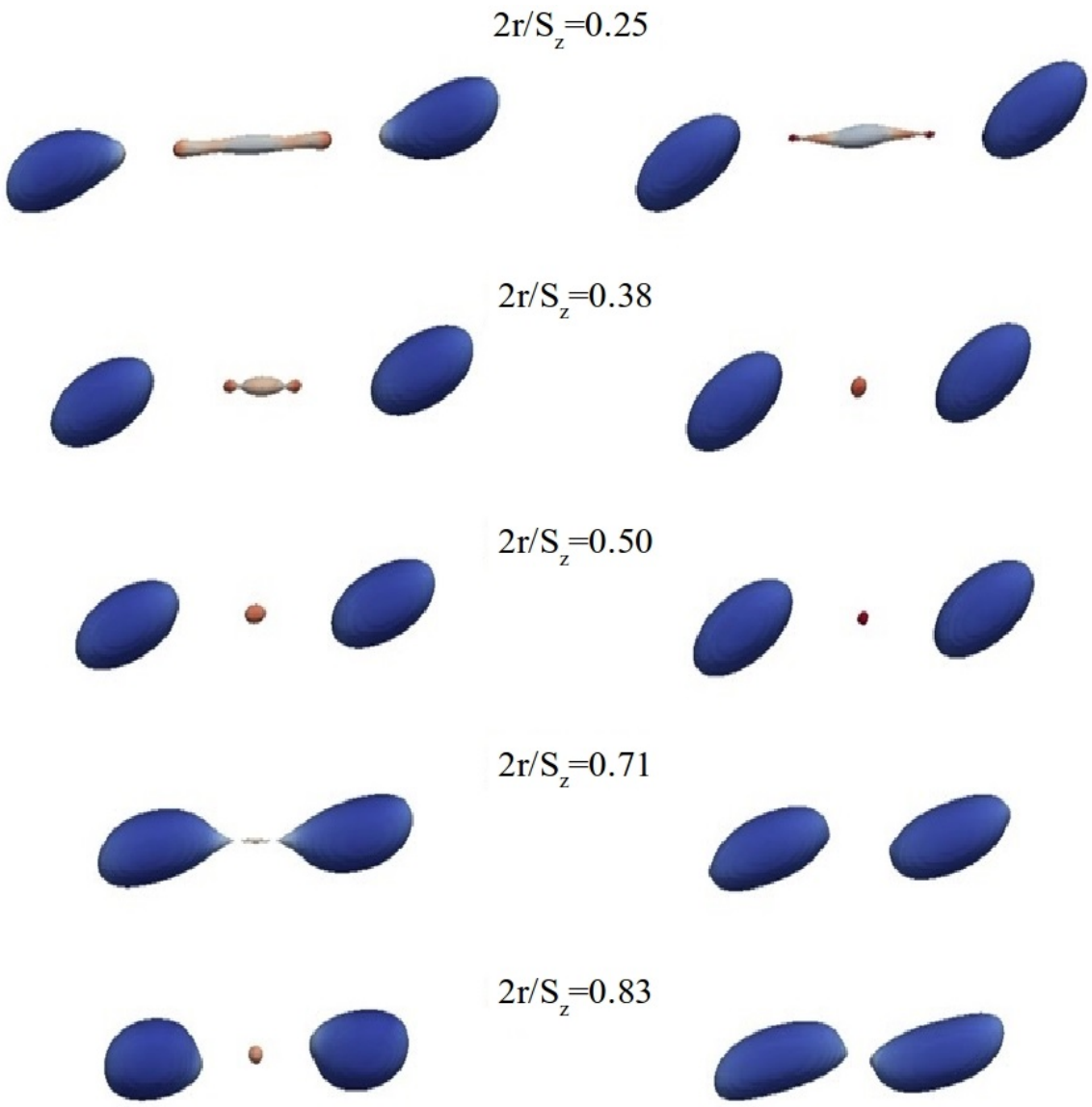

Figure 16: breakup of the droplet into daughter, satellite, and sub-satellite droplets for supercritical cases of table 3. The color contours are pressure on the droplet surface. The left column is related to droplet breakups of supercritical cases of the higher steady-state region. Right column is related to droplet breakups of supercritical cases of lower steady-state region. The videos of the deformation and breakup processes of the most confined cases ($2r/S_z = 0.83$) are provided in supplementary videos (supplementary videos 1 and 2 regarding the breakups of supercritical cases of the higher steady-state region and supplementary videos 3 and 4 regarding the breakups of supercritical cases of the lower steady-state region) for oblique and side views. In these videos time is being non-dimensionalized as $3t\dot{\gamma}$ and the color contours represent the velocity magnitude on the droplets surface with the same colourmap as represented in figure 4

deformation of the droplet without breakup. According to this figure, for a constant capillary number more than the critical value, there are two critical viscosity ratios, one smaller than the other. For smaller critical viscosity ratio, increasing the λ will lead to breakup while for bigger critical viscosity ratios, decreasing the λ will lead to breakup. Simulations without the presence of confinement effect of walls, performed so far in this paper, are in agreement with Grace curve. Our simulations in creeping flow condition presented in figure 3 ($\lambda = 1$, Ca=0.05, 0.1, 0.2, 0.3 and 0.4) as well as simulations presented in figure 10 (Ca=0.2 and λ=0.28, 1.2 and 1.9), which all ended in steady-state deformation of the droplet, are in lower part of Grace curve (steady-state region) and simulation of figure 4 ($\lambda = 1$ and Ca=0.42), ended in breakup of the droplet, locates in the upper part of Grace curve (breakup region).

Despite the important information provided in this graph, the walls confinement effect is not taken into account. Figure 12 (right) illustrates the findings of Janssen et al. [48] on the effect of walls confinement ratio on critical capillary number. Despite the important information provided in this graph, the effect of different viscosity ratios is not taken into account. Although combined with the Grace curve, these two graphs provide essential information regarding the critical capillary number in different viscosity and walls confinement ratios; there is a need to specify the effect of viscosity ratio on the walls critical confinement ratio.

In this section, we study the effect of viscosity ratio on walls critical confinement ratio in droplet deformation and breakup for a constant capillary number of 0.3 and Reynolds number of 1.0. We have selected Ca=0.3 so that the droplet could undergo both steady-state deformation and breakup in the considered range of governing parameters. A simulation with a decidedly smaller capillary number would not exhibit breakup, and a simulation with a more prominent capillary number would not undergo the steady-state deformation, and as a result, we would not be able to extract the whole diversity of physical phenomena as extracted in this section. We perform a batch of simulations, where the walls confinement ratio and viscosity ratio of the droplet to the matrix are changed systematically. For each confinement ratio, we look for two values of critical viscosity ratios, one smaller than the other. Considering the conclusion of the Grace curve, for the lower critical viscosity ratio (λ_{cr}^{l}), decreasing the λ value will lead to steady-state deformation, and increasing the λ value will lead to the breakup of the droplet. Although for the higher critical viscosity ratio (λ_{cr}^{h}), we expect opposite behavior, as ascending from λ value is supposed to lead to steady-state deformation and descending from it is supposed to lead to breakup of the droplet.

In order to find the λ_{cr}^{l} and λ_{cr}^{h} as a function of $2r/S_z$, for each chosen value of walls confinement ratio, we were starting the simulation with arbitrary λs, searching for values where result in breakup of the

droplet. We then gradually descend (ascent) from this value until simulation winds up in steady-state, with no breakup, to find λ_{cr}^{l} (λ_{cr}^{h}). This process was done for walls confinement ratios of $2r/S_z$=0.25, 0.38, 0.5, 0.71 and 0.83. A domain length of $S_x = 16r$ is used to guarantee that the droplet is not going to collide with its own image through periodic boundaries, and also to ensure an acceptable uniform velocity profile at the location of periodic boundaries. For each critical viscosity ratio found, there is one subcritical λ (λ_{sub}, leading to steady-state deformation) and one supercritical λ (λ_{super}, leading to breakup). For the simulations performed, these values are extracted and presented in table 3 as well as steady-state values of D, θ, $L_p/2r$ and $W/2r$ for subcritical cases.

Figure 13 illustrates the data provided in table 3. In this figure, it is noticeable that two steady-state regions exist, one corresponding to λ values smaller than λ_{cr}^{l} (hereinafter refereed to as *lower steady-state* region) and another corresponding to λ values bigger than λ_{cr}^{h} (hereinafter refereed to as *higher steady-state* region). All the simulations in these two areas resulted in steady-state deformation of the droplet. In the area between these two regions, there is a breakup zone in which simulations in this area, resulted in the breakup of the droplet.

As mentioned before and as can be seen in the Grace curve (fig. 12), in creeping flow conditions without the effect of walls confinement, for λ values higher than 4, simulation always results in steady-state deformation. Although In our study, simulations with λ values as high as λ=13 ended-up in breakup. We believe this is associated with effect of walls confinement, eventhough slightly higher Reynolds number in our cases is affecting as well.

According to figure 13, in the *lower steady-state* region, by increasing the confinement ratio, the critical viscosity ratio monotonically increases. However, for the *higher steady-state* region, starting from $2r/S_z$=0.25, increasing the confinement ratio up to $2r/S_z \approx 0.45$, decreases the λ_{cr}^{h}, and after that, rapidly increases the λ_{cr}^{h}.

The results of figure 13 combined with the Grace curve and the findings of Janssen et al. [48] provide important information on the binary relation between viscosity ratio-walls critical confinement ratio, critical capillary number-viscosity ratio, and critical capillary number-confinement ratio, respectively. These information are interesting and could be used to gain an understanding of the critical Grace number in different confinement ratios.

In order to gain a better understanding of the introduced graph, the steady-state shape of the droplet, streamlines of the flow inside of the droplet and the color contour of the vorticity magnitude all in x-z at $y = S_y/2$ plane for subcritical cases in different confinement ratios are presented in figure 14. In this

figure, the left column corresponds to the subcritical cases of the *higher steady-state* region and right column corresponds to subcritical cases of the *lower steady-state* region. It is plain to see that by increasing the confinement ratio, the droplet leans more towards the flow direction. This can be seen quantitatively in the data provided in table 3 in which for example in cases with $2r/S_z$=0.25, the value of inclination angle for subcritical cases in *lower and higher steady-state* regions are 25.32°and 17.25°, respectively. These values are bigger than the equivalent values in confinement ratio of $2r/S_z$=0.71 which are 11.16°and 11.03°. In all the cases in both *lower and higher steady-state* regions, by increasing the confinement ratio, the droplet stretches more in the flow direction and as a result, the width of the droplet decreases (see for example parameters Lp/2r and W/2r presented in table 3).

According to figure 14, and also information provided in table 3, in each confinement ratio, the value of inclination angle for subcritical cases in *lower steady-state* region is higher than the same parameter in *higher steady-state* region. In another word, in each confinement ratio, in subcritical cases, for viscosity ratios in the *lower steady-state* region, the droplet leans more towards the flow direction compared with the viscosity ratios in the *higher steady-state* region. Also in each confinement ratio, the Lp/2r parameter which describes how much the droplet is stretched in the flow direction, for subcritical cases in the *lower steady-state* region is higher than subcritical cases in the *higher steady-state* region.

According to figure 14, for five cases, there are two vortices inside of the droplet, and for the rest, there are only one. The cases with two vortices inside of the droplet are ($2r/S_z$,λ)=(0.25, 0.2) and all the cases with $2r/S_z$=0.71 and 0.83. We suppose that for the case of ($2r/S_z$,λ)=(0.25, 0.2), this ratio (λ) is small enough to allow the existence of two vortices inside of the drop. For cases with $2r/S_z$=0.71 and 0.83, the existence of two vortices inside of the droplet could be linked to the effect of higher confinement ratios and the suppressing effect of the walls. In this figure, for cases in the *lower steady-state* region (right column of images), the vorticity magnitude is higher compared to the relative case in the *higher steady-state* region (left column of images). This could be associated with lower viscosity ratio of the cases of right column compared with the relative cases in the left column.

For cases introduced in figure 14, time-dependent changes of Lp/2r, W/2r and D parameters are presented in figure 15. It is clear to see that simulations in these cases have reached steady-state over time. In this figure, for each confinement ratio, the results of simulations with two viscosities of λ_l and λ_h are similar to each other, except for cases (d) and (e). In the case (d), the Lp/2r parameter of the droplet in subcritical case of the *lower steady-state* region is approximately 23% more than its equivalent case in subcritical case of the *higher steady-state* region. In case (e) this difference in the Lp/2r parameter between *lower and*

higher steady-state regions increases to 45%. This difference which can be seen in figure 14 as well, could be associated with the bigger difference in λ values in subcritical cases compared with the other cases. For example, for subcritical cases in the domain with $2r/S_z$=0.71, the difference between λ^l_{sub} and λ^h_{sub} is 3.6, while this value for cases in domain with $2r/S_z$=0.50 is only 1.35.

Figure 16 illustrates the droplet breakup outcomes for supercritical cases mentioned in table 3 for different confinement ratios. According to this figure, figure 14 and information provided in table 3, eventhough for subcritical cases, by increasing the confinement ratio, droplet stretches more towards the flow direction, for the relative supercritical cases, by increasing the confinement ratio, the droplet stretches less before breaking-up. In another word, for smaller confinement ratios ($2r/S_z$=0.25, 0.38) the breakup mechanism is elongative end-pinching while increasing the confinement ratio changes this mechanism to mid-point-pinching. It is noteworthy that the presented results in this section are regarding a constant capillary number of 0.3, and the effect of variation of the capillary number on these results is yet to be studied.

5. Conclusion

A finite-volume conservative level-set based method was utilized to numerically study the effect of viscosity ratio on walls critical confinement ratio for deformation and breakup of a droplet in shear flow. To do so, first, we selected validation test cases that concern the physical behaviours appearing in this phenomena, i.e. breakup of a droplet into satellite and sub-satellite droplets, deformation of a droplet under walls confinement effect and deformation of a droplet in different viscosity ratios. In all the cases, a very good agreement was seen between the results extracted in the current study and the data available on literature. In order to study the effect of viscosity ratio on walls critical confinement ratio, we have selected a small Reynolds number of 1.0 and a constant capillary number of 0.3. We found out that for each confinement ratio, there are two critical viscosity ratios. These two viscosity ratios create two steady-state regions and one breakup region between them. We further analyzed these regions by studying the droplet deformation and breakup parameters in these zones.

The insights gained from the research in this paper on the effect of viscosity ratio on walls critical confinement ratio provide a clear roadmap to steady-state and breakup regions of droplets in shear. This information is valuable in more effective design of future droplet-based microfluidic devices, reactive dispersions, emulsification process, morphology development of blends and Lab-on-a-Chip systems for individual purposes with methods discussed in this paper, namely, by adjusting the viscosity or confinement ratios of the existing shear flow to the appropriate values to control the droplet volume. For example, the pro-

vided information on the existence and relation of two steady-state and one breakup regions can be used to quantify emulsions stability by analyzing the droplet size spectrum in the emulsion.

Acknowledgments

This work has been financially supported by the *Ministerio de Economía y Competitividad, Secretaría de Estado de Investigación, Desarrollo e Innovación*, Spain (ENE2015-70672-P). A. Amani acknowledges the financial support of an FI research scholarship by the *Agència de Gestió d'Ajuts Universitaris i de Recerca (AGAUR) of Generalitat de Catalunya* (2016 FI_B 01059). N. Balcázar acknowledges the financial support of the *Programa Torres Quevedo* (PTQ-14-07186). The authors thankfully acknowledge the computer resources at Altamira and the technical support provided by Instituto de Física de Cantabria - Universidad de Cantabria (RES-FI-2018-3-0045).

Appendix A. The effect of variable CLS parameters on the results

The effect of variable CLS parameters of C_τ and α on final results is studied through a set of numerical simulations. These two parameters are introduced in equations 14 and 10, respectively. The results including time varying D, Lp/2r and W/2r parameters and steady-state shape of the droplet are presented in figures B.17 and B.18, for cases with Re=0.1, Ca=0.3, λ=1 in a domain with $(S_x, S_y, S_z) = (8r, 4r, 8r)$ with the grid size of $h = 2r/25$. In the cases of figure B.17, for a constant value of C_τ=0.025, three different values of α=0.0, 0.05 and 0.10 are tested. In the cases of figure B.18, for a constant value of α=0.0, three different values of C_τ=0.01, 0.025 and 0.050 are tested. The selected values include the boundaries of the proposed range for these parameters. According to these results, the variation of C_τ and α, has negligible influence on deformation of the droplet, thus any value in the proposed range could be used. However, According to figure B.18 (left), since the values of droplet deformation parameter (D) for C_τ=0.01 and 0.025 are very close to each other, we believe in this sub-range ([0.01,0.025]), the effect of this parameter would even be smaller and almost close to zero. As a result, an arbitrary value in this sub-range would be an appropriate choice which we select C_τ=0.015. For all the simulations throughout this paper, values of 0.015 and 0.0 were set for C_τ and α, respectively.

In each iteration, droplet's mass conservation error is calculated using $\Delta M = (M_t - M_0)/M_0$, where M_0 is droplet's initial mass and M_t is droplet's mass at time t. In all the simulations of this research, droplet's mass conservation error is in the order of $O(10^{-12})$. Figure B.19 presents the time variation of mass conservation error of the droplet for cases with Re=0.1 and λ=1, and four capillary numbers of 0.1,

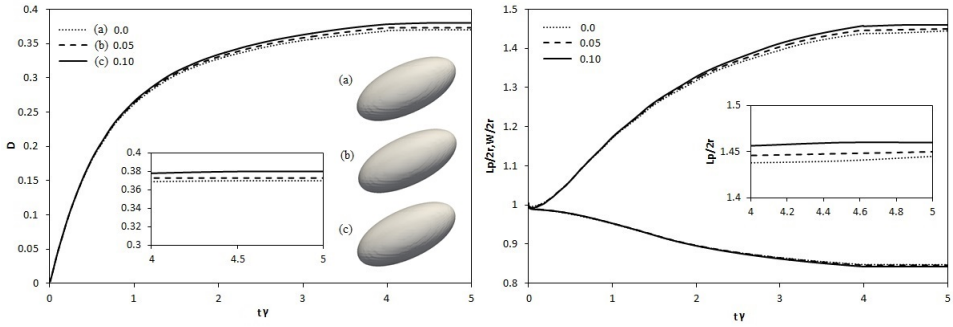

Figure B.17: Left: Taylor deformation parameter (D), right: $L_p/2r$ and W/2r parameters vs. $t\dot{\gamma}$ for subcritical cases with Re=0.1, Ca=0.3 and λ=1 all in a domain with $(S_x, S_y, S_z) = (8r, 4r, 8r)$ and grid size of $h = 2r/25$. All the cases have $C_\tau = 0.025$. Three different values of α = 0.0, 0.05 and 0.10 are tested.

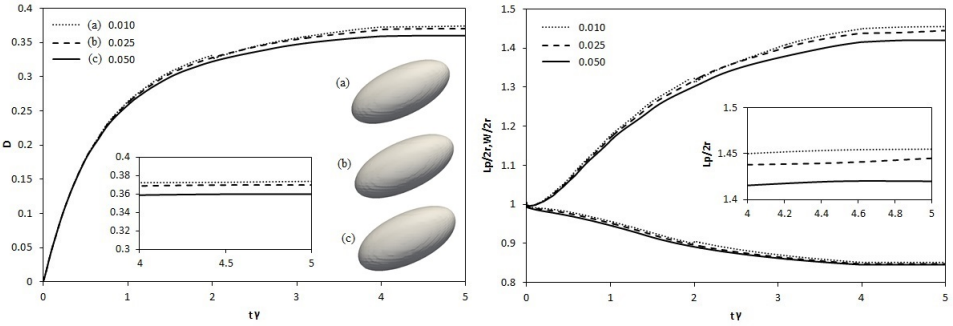

Figure B.18: Left: Taylor deformation parameter (D), right: $L_p/2r$ and W/2r parameters vs. $t\dot{\gamma}$ for subcritical cases with Re=0.1, Ca=0.3 and λ=1 all in a domain with $(S_x, S_y, S_z) = (8r, 4r, 8r)$ and grid size of $h = 2r/25$. All the cases have $\alpha = 0.0$. Three different values of C_τ = 0.01, 0.025 and 0.050 are tested.

0.2, 0.3 and 0.4, all in a domain with the grid size of $h = 2r/25$. Evidently, the mass conservation error of droplet in all the cases has converged to the order of $O(10^{-12})$.

Appendix B. Harmonic Vs. Linear Average of Viscosity

In order to compare the accuracy of harmonic versus linear average of viscosity, a two-dimensional test case of oscillation of a droplet in an adjacent matrix in x-y plane is studied. The domain is a square with the side length of 8r with the droplet placed in its center, (x_0, y_0). At time t=0, an initial velocity as following

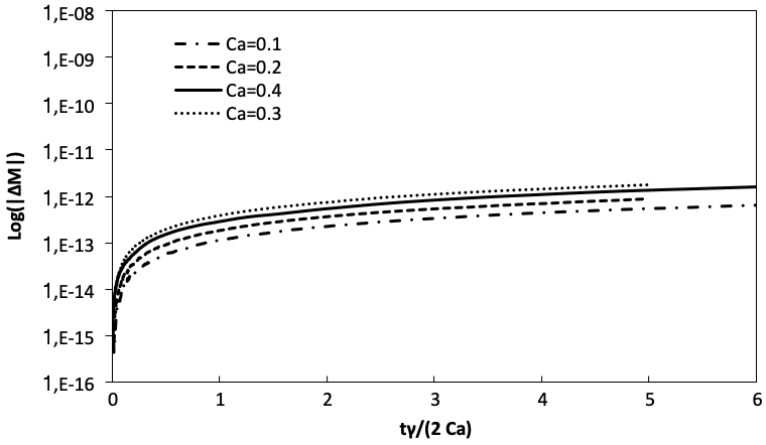

Figure B.19: The evolution in the mass conservation error of the droplet for cases all with Re=0.1 and λ=1 in a domain with the grid size of $h = 2r/25$. The results of the simulation with four different capillary numbers of 0.1, 0.2, 0.3 and 0.4 are presented. ΔM for the droplet is $(M_t - M_0)/M_0$, where M_0 is droplet's initial mass and M_t is the mass at time t.

is applied to the droplet, causing an oscillation in its deformation:

$$U = u_0 \frac{x - x_0}{2r} \tag{B.1}$$

$$V = -u_0 \frac{y - y_0}{2r} \tag{B.2}$$

where U and V are velocities in x and y directions, respectively. Four different grid sizes used to solve this problem are h=r/10, 2r/25, r/15 and r/20, where the results of the finest grid are used as the reference to extract the order of accuracy convergence in space. Two different interpolation methods of linear and harmonic are applied in calculations of viscosity. Time is non-dimensionalized with $t^* = r/u_0$. A constant non-dimensional time-step of $dt' = dt/t^* = 7 \times 10^{-4}$ is used in all the simulations. The physical properties of the droplet and matrix are presented in table B.4 where Weber and Reynolds are defined as follows:

$$We = \frac{\rho_d u_0^2 r}{\sigma} \tag{B.3}$$

$$Re = \frac{\rho_d u_0 r}{\mu_D} \tag{B.4}$$

Simulations are performed until t*=10. The radial expansion of the droplet in y-direction as a function of time for these cases are presented in figure B.20.

Table B.4: Flow parameters of the 2D droplet oscillation test case

ρ_d/ρ_m	μ_d/μ_m	We	Re
666.08	119.08	5.0	6.25

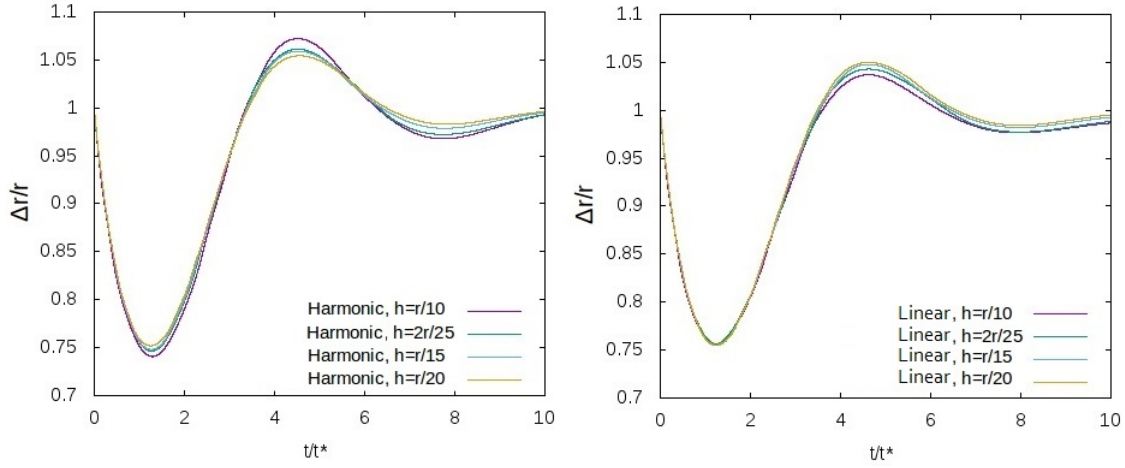

Figure B.20: Time variation of non-dimensionalized radial expansion of the droplet in y-direction for cases with linear and harmonic interpolation of the viscosity in domain with different grid sizes.

The U component of velocity in the centerline x-direction at $t' = 10$ is extracted as comparison criteria. The results of cases with h=r/20 for linear and harmonic cases are used as the reference of linear and harmonic cases, respectively. The first-norm of error for each case is extracted and used to calculate the convergence of the solution as $L_1 = \sum_i |e_i|$, where e_i is the point-wise error of each cell compared with its reference. According to the extracted results, the linear interpolation of viscosity has the convergence rate of 2.03 in space, while the same value for results of harmonic interpolation is 2.61.

Appendix C. Momentum Convergence Analysis

In order to evaluate the accuracy convergence of momentum equation in time, a 2D channel flow problem with the length of S_x and height of $S_y = H$ in x and y directions, is solved. The initial configuration of the domain is illustrated in figure C.21. A periodic boundary condition is applied in X direction and no-slip boundary condition in Y. Numerical parameters to fully define this problem are presented in table C.5. For this problem, analytical exact solution would be as follows:

Table C.5: Flow parameters of the 2D channel test case

ρ_1/ρ_2	μ_1/μ_2	σ	$\partial P/\partial x$
1.0	10	20	0.2

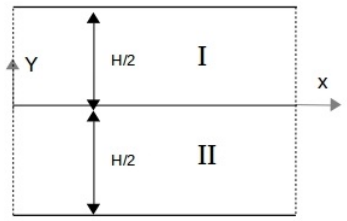

Figure C.21: Schematic of the 2D channel flow problem.

$$V_x(y) = \frac{\partial P}{\partial x}\frac{h^2}{2\mu_i}\Big[\frac{2\mu_i}{\mu_1+\mu_2} + \frac{\mu_1-\mu_2}{\mu_1+\mu_2}(\frac{y}{h}) - (\frac{y}{h})^2\Big] \tag{C.1}$$

where $i \in \{I, II\}$ determines the region of the fluid. Numerical simulations are done for enough long time to reach steady-state (t=30.0 s). Three different time steps of $dt = 2\times10^{-5}, 4\times10^{-5}$ and 8×10^{-5} for solutions in a domain with grid size of h=H/40 are used. Figure C.22 represent the variation of x-direction velocity profile in y direction ($V_x(y)$) for cases with different time steps, along with the analytical exact solution.

In each case, x-direction velocity profile at t=30.0 is extracted to compare the results. The Analytical solution is used as the reference. The infinity-norm of error for each case is extracted and used to calculate the convergence of the solution as $L_\infty = max(|e_i|)$, where e_i is the point-wise error of each cell compared with its reference. Figure C.23 illustrates the L_∞ of the error for different time steps. As can be seen, the convergence of error for this test case is almost 2.

References

1. Tufano C, Peters GWM, Meijer HEH. Confined flow of polymer blends. *Langmuir* 2008;24(9):4494–505. URL: `https://doi.org/10.1021/la7036636`. doi:`10.1021/la7036636`. `arXiv:https://doi.org/10.1021/la7036636`; pMID: 18348582.
2. Stone H, Stroock A, Ajdari A. Engineering flows in small devices: Microfluidics toward a lab-on-a-chip. *Annual Review of Fluid Mechanics* 2004;36(1):381–411. URL: `https://doi.org/10.1146/annurev.fluid.36.050802.122124`. doi:`10.1146/annurev.fluid.36.050802.122124`. `arXiv:https://doi.org/10.1146/annurev.fluid.36.050802.122124`.
3. Komrakova A, Shardt O, Eskin D, Derksen J. Lattice boltzmann simulations of drop deformation and breakup in shear flow. *International Journal of Multiphase Flow* 2014;59:24 – 43. URL: `http://www.sciencedirect.com/science/article/pii/S0301932213001547`. doi:`http://dx.doi.org/10.1016/j.ijmultiphaseflow.2013.10.009`.

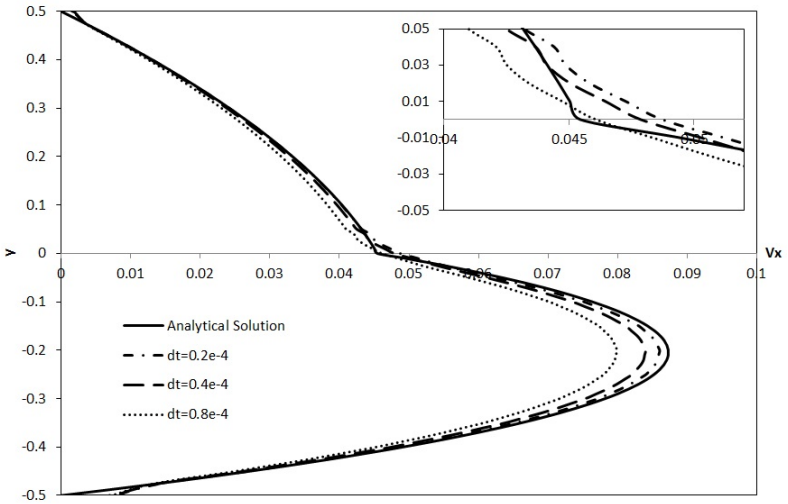

Figure C.22: Variation of V_x velocity profile in y direction for cases with different time steps, along with the exact solution.

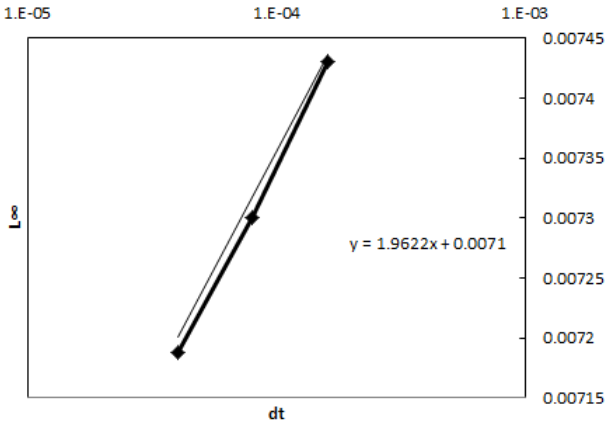

Figure C.23: L_∞ of the error in $V_X(y)$ compared with the analytical solution, Vs. time step of the simulations.

4. Mason TG, Bibette J. Shear Rupturing of Droplets in Complex Fluids. *Langmuir* 1997;13(17):4600–13. URL: http://pubs.acs.org/doi/abs/10.1021/la9700580. doi:10.1021/la9700580.
5. Gounley J, Boedec G, Jaeger M, Leonetti M. Influence of surface viscosity on droplets in shear flow. *J Fluid Mech* 2016;791:464–94. URL: http:/www.cambridge.org/core/terms.{%}5Cnhttp://dx.doi.org/10.1017/jfm.2016.39. doi:10.1017/jfm.2016.39.
6. AbouHassan A, Sandre O, Cabuil V. Microfluidics in inorganic chemistry. *Angewandte Chemie International Edition* 2010;49(36):6268–86. URL: https://onlinelibrary.wiley.com/doi/abs/10.1002/anie.200904285. doi:10.1002/anie.200904285.
7. Li L, Fu Q, Kors CA, Stewart L, Nollert P, Laible PD, Ismagilov RF. A plug-based microfluidic system for dispensing lipidic cubic phase (lcp) material validated by crystallizing membrane proteins in lipidic mesophases. *Microfluidics and Nanofluidics* 2010;8(6):789–98. URL: https://doi.org/10.1007/s10404-009-0512-8. doi:10.1007/s10404-009-0512-8.
8. Rowat AC, Bird JC, Agresti JJ, Rando OJ, Weitz DA. Tracking lineages of single cells in lines using a microfluidic device. *Proceedings of the National Academy of Sciences* 2009;106(43):18149–54. URL: http://www.pnas.org/content/106/43/18149. doi:10.1073/pnas.0903163106. arXiv:http://www.pnas.org/content/106/43/18149.full.pdf.
9. Theberge A, Courtois F, Schaerli Y, Fischlechner M, Abell C, Hollfelder F, Huck W. Microdroplets in microfluidics: An evolving platform for discoveries in chemistry and biology. *Angewandte Chemie International Edition* 2010;49(34):5846–68. URL: https://onlinelibrary.wiley.com/doi/abs/10.1002/anie.200906653. doi:10.1002/anie.200906653. arXiv:https://onlinelibrary.wiley.com/doi/pdf/10.1002/anie.200906653.
10. Vyawahare S, Griffiths AD, Merten CA. Miniaturization and parallelization of biological and chemical assays in microfluidic devices. *Chemistry Biology* 2010;17(10):1052 –65. URL: http://www.sciencedirect.com/science/article/pii/S1074552110003510. doi:https://doi.org/10.1016/j.chembiol.2010.09.007.
11. Seemann R, Brinkmann M, Pfohl T, Herminghaus S. Droplet based microfluidics. *Reports on Progress in Physics* 2012;75(1):016601. URL: http://stacks.iop.org/0034-4885/75/i=1/a=016601.
12. Kennedy M, Pozrikidis C, Skalak R. Motion and deformation of liquid drops, and the rheology of dilute emulsions in simple shear flow. *Computers and Fluids* 1994;23(2):251 –78. URL: http://www.sciencedirect.com/science/article/pii/004579309490040X. doi:http://dx.doi.org/10.1016/0045-7930(94)90040-X.
13. Taylor GI. The viscosity of a fluid containing small drops of another fluid. *Proceedings of the Royal Society of London A: Mathematical, Physical and Engineering Sciences* 1932;138(834):41–8. URL: http://rspa.royalsocietypublishing.org/content/138/834/41. doi:10.1098/rspa.1932.0169. arXiv:http://rspa.royalsocietypublishing.org/content/138/834/41.full.pdf.
14. Taylor GI. The formation of emulsions in definable fields of flow. *Proceedings of the Royal Society of London A: Mathematical, Physical and Engineering Sciences* 1934;146(858):501–23. URL: http://rspa.royalsocietypublishing.org/content/146/858/501. doi:10.1098/rspa.1934.0169. arXiv:http://rspa.royalsocietypublishing.org/content/146/858/501.full.pdf.
15. Rallison JM. The Deformation of Small Viscous Drops and Bubbles in Shear Flows. *Annual Review of Fluid Mechanics* 1984;16(1):45–66. URL: http://dx.doi.org/10.1146/annurev.fl.16.010184.000401. doi:10.1146/annurev.fl.16.010184.000401.
16. Stone HA. Dynamics of drop deformation and breakup in viscous fluids. *Annual Review of Fluid Mechanics* 1994;26(1):65–102. URL: http://dx.doi.org/10.1146/annurev.fl.26.010194.000433. doi:10.1146/annurev.fl.26.010194.000433.

arXiv:http://dx.doi.org/10.1146/annurev.fl.26.010194.000433.

17. Cristini V, Renardy Y. Scalings for droplet sizes in shear-driven breakup: non-microfluidic ways to monodisperse emulsions. *Fluid Dyn Mater Process* 2006;2(2):77–94.
18. Marks CR. Drop breakup and deformation in sudden onset strong flows 1998;.
19. Bentley BJ, Leal LG. An experimental investigation of drop deformation and breakup in steady, two-dimensional linear flows. *Journal of Fluid Mechanics* 1986;167:241–83. URL: http://journals.cambridge.org/article_S0022112086002811. doi:10.1017/S0022112086002811.
20. Vananroye A, Van Puyvelde P, Moldenaers P. Structure development in confined polymer blends: steady-state shear flow and relaxation. *Langmuir* 2006;22(5):2273–80.
21. Sibillo V, Pasquariello G, Simeone M, Cristini V, Guido S. Drop deformation in microconfined shear flow. *Phys Rev Lett* 2006;97:054502. URL: http://link.aps.org/doi/10.1103/PhysRevLett.97.054502. doi:10.1103/PhysRevLett.97.054502.
22. Shapira M, Haber S. Low reynolds number motion of a droplet between two parallel plates. *International Journal of Multiphase Flow* 1988;14(4):483 – 506. URL: http://www.sciencedirect.com/science/article/pii/0301932288900249. doi:http://dx.doi.org/10.1016/0301-9322(88)90024-9.
23. Shapira M, Haber S. Low reynolds number motion of a droplet in shear flow including wall effects. *International Journal of Multiphase Flow* 1990;16(2):305 –21. URL: http://www.sciencedirect.com/science/article/pii/030193229090061M. doi:http://dx.doi.org/10.1016/0301-9322(90)90061-M.
24. Roths T, Friedrich C, Marth M, Honerkamp J. Dynamics and rheology of the morphology of immiscible polymer blends – on modeling and simulation. *Rheologica Acta* 2002;41(3):211–22. URL: https://doi.org/10.1007/s003970100189. doi:10.1007/s003970100189.
25. van der Sman R, van der Graaf S. Emulsion droplet deformation and breakup with lattice boltzmann model. *Computer Physics Communications* 2008;178(7):492 – 504. URL: http://www.sciencedirect.com/science/article/pii/S0010465507004675. doi:http://dx.doi.org/10.1016/j.cpc.2007.11.009.
26. Richardson S. Two-dimensional bubbles in slow viscous flows. *Journal of Fluid Mechanics* 1968;33:475–93. URL: http://journals.cambridge.org/article_S0022112068001461. doi:10.1017/S0022112068001461.
27. Toose E, Geurts B, Kuerten J. A boundary integral method for two-dimensional (non)-newtonian drops in slow viscous flow. *Journal of Non-Newtonian Fluid Mechanics* 1995;60(2-3):129 –54. URL: http://www.sciencedirect.com/science/article/pii/0377025795013863. doi:http://dx.doi.org/10.1016/0377-0257(95)01386-3.
28. Minale M. A phenomenological model for wall effects on the deformation of an ellipsoidal drop in viscous flow. *Rheologica Acta* 2008;47(5):667–75. URL: http://dx.doi.org/10.1007/s00397-007-0237-0. doi:10.1007/s00397-007-0237-0.
29. Kwak S, Pozrikidis C. Adaptive triangulation of evolving, closed, or open surfaces by the advancing-front method. *Journal of Computational Physics* 1998;145(1):61 – 88. URL: http://www.sciencedirect.com/science/article/pii/S0021999198960302. doi:http://dx.doi.org/10.1006/jcph.1998.6030.
30. Janssen PJA, Anderson PD. Boundary-integral method for drop deformation between parallel plates. *Physics of Fluids* 2007;19(4):043602. URL: http://scitation.aip.org/content/aip/journal/pof2/19/4/10.1063/1.2715621. doi:http://dx.doi.org/10.1063/1.2715621.
31. Pozrikidis C. Boundary Integral and Singularity Methods for Linearized Viscous Flow (Cambridge Texts in Applied Mathematics). Cambridge University Press; 1992. ISBN 0521406935. URL: http://www.amazon.com/exec/obidos/redirect?

tag=citeulike07-20&path=ASIN/0521406935.

32. Xi H, Duncan C. Lattice boltzmann simulations of three-dimensional single droplet deformation and breakup under simple shear flow. *Phys Rev E* 1999;59:3022–6. URL: http://link.aps.org/doi/10.1103/PhysRevE.59.3022. doi:10.1103/PhysRevE.59.3022.
33. Shan X, Chen H. Lattice boltzmann model for simulating flows with multiple phases and components. *Phys Rev E* 1993;47:1815–9. URL: http://link.aps.org/doi/10.1103/PhysRevE.47.1815. doi:10.1103/PhysRevE.47.1815.
34. Li J, Renardy YY, Renardy M. Numerical simulation of breakup of a viscous drop in simple shear flow through a volume-of-fluid method. *Physics of Fluids* 2000;12(2).
35. Renardy YY, Cristini V. Effect of inertia on drop breakup under shear. *Physics of Fluids* 2001;13(1).
36. Renardy Y, Cristini V, Li J. Drop fragment distributions under shear with inertia. *International Journal of Multiphase Flow* 2002;28(7):1125 –47. URL: http://www.sciencedirect.com/science/article/pii/S0301932202000228. doi:http://dx.doi.org/10.1016/S0301-9322(02)00022-8.
37. Khismatullin DB, Renardy Y, Cristini V. Inertia-induced breakup of highly viscous drops subjected to simple shear. *Physics of Fluids* 2003;15(5).
38. Balcázar N, Lehmkuhl O, Jofre L, Rigola J, Oliva A. A coupled volume-of-fluid/level-set method for simulation of two-phase flows on unstructured meshes. *Computers and Fluids* 2016;124:12 – 29. Special Issue for ICMMES-2014.
39. Verhulst K, Cardinaels R, Moldenaers P, Renardy Y, Afkhami S. Influence of viscoelasticity on drop deformation and orientation in shear flow Part 1. Stationary states. *J Non-Newtonian Fluid Mech* 2009;156:29–43. doi:10.1016/j.jnnfm.2008.06.007.
40. Mukherjee S, Sarkar K. Effects of viscosity ratio on deformation of a viscoelastic drop in a Newtonian matrix under steady shear. *J Non-Newtonian Fluid Mech* 2009;160:104–12. doi:10.1016/j.jnnfm.2009.03.007.
41. Hsu AS, Leal GL. Deformation of a viscoelastic drop in planar extensional flows of a Newtonian fluid. *J Non-Newtonian Fluid Mech* 2009;160:176–80. doi:10.1016/j.jnnfm.2009.03.004.
42. Ioannou N, Liu H, Oliveira M, Zhang Y. Droplet dynamics of newtonian and inelastic non-newtonian fluids in confinment. *Micromachines* 2017;8(2):57. URL: http://www.mdpi.com/2072-666X/8/2/57. doi:10.3390/mi8020057.
43. Balcázar N, Lehmkuhl O, Jofre L, Oliva A. Level-set simulations of buoyancy-driven motion of single and multiple bubbles. *International Journal of Heat and Fluid Flow* 2015;56:91 – 107. URL: http://www.sciencedirect.com/science/article/pii/S0142727X15000867. doi:http://dx.doi.org/10.1016/j.ijheatfluidflow.2015.07.004.
44. Balcázar N, Jofre L, Lehmkuhl O, Castro J, Rigola J. A finite-volume/level-set method for simulating two-phase flows on unstructured grids. *International Journal of Multiphase Flow* 2014;64:55 – 72. URL: http://www.sciencedirect.com/science/article/pii/S030193221400072X. doi:http://dx.doi.org/10.1016/j.ijmultiphaseflow.2014.04.008.
45. Amani A, Balcázar N, Gutiérrez E, Oliva A. Numerical study of binary droplets collision in the main collision regimes. *Chemical Engineering Journal* 2019;370:477 –98. URL: http://www.sciencedirect.com/science/article/pii/S1385894719306631. doi:https://doi.org/10.1016/j.cej.2019.03.188.
46. Balcázar N, Castro J, Rigola J, Oliva A. Dns of the wall effect on the motion of bubble swarms. *Procedia Computer Science* 2017;108(Supplement C):2008 –17. URL: http://www.sciencedirect.com/science/article/pii/S1877050917306142. doi:https://doi.org/10.1016/j.procs.2017.05.076; international Conference on Computational Science, ICCS 2017, 12-14 June 2017, Zurich, Switzerland.
47. Vananroye A, Van Puyvelde P, Moldenaers P. Effect of confinement on droplet breakup in sheared

emulsions. *Langmuir* 2006;22(9):3972–4. URL: http://dx.doi.org/10.1021/la060442+. doi:10.1021/la060442+. arXiv:http://dx.doi.org/10.1021/la060442+; pMID: 16618134.

48. Janssen PJA, Vananroye A, Puyvelde PV, Moldenaers P, Anderson PD. Generalized behavior of the breakup of viscous drops in confinements. *Journal of Rheology* 2010;54(5):1047–60. URL: http://dx.doi.org/10.1122/1.3473924. doi:10.1122/1.3473924. arXiv:http://dx.doi.org/10.1122/1.3473924.
49. Olsson E, Kreiss G. A conservative level set method for two phase flow. *Journal of Computational Physics* 2005;210(1):225 –46. URL: http://www.sciencedirect.com/science/article/pii/S0021999105002184. doi:http://dx.doi.org/10.1016/j.jcp.2005.04.007.
50. Balcázar N, Lehmkuhl O, Rigola J, Oliva A. A multiple marker level-set method for simulation of deformable fluid particles. *International Journal of Multiphase Flow* 2015;74:125 –42. URL: http://www.sciencedirect.com/science/article/pii/S0301932215001019. doi:http://dx.doi.org/10.1016/j.ijmultiphaseflow.2015.04.009.
51. Brackbill J, Kothe D, Zemach C. A continuum method for modeling surface tension. *Journal of Computational Physics* 1992;100(2):335 –54. URL: http://www.sciencedirect.com/science/article/pii/002199919290240Y. doi:http://dx.doi.org/10.1016/0021-9991(92)90240-Y.
52. Chorin AJ. Numerical solution of the navier-stokes equations. *Mathematics of computation* 1968;22(104):745–62.
53. Gottlieb S, Shu CW. Total variation diminishing runge-kutta schemes. *Mathematics of computation of the American Mathematical Society* 1998;67(221):73–85.
54. Armfield S, Street R. An analysis and comparison of the time accuracy of fractional-step methods for the navier-stokes equations on staggered grids. *International Journal for Numerical Methods in Fluids* 2002;38(3):255–82. URL: http://dx.doi.org/10.1002/fld.217. doi:10.1002/fld.217.
55. Kim J, Moin P. Application of a fractional-step method to incompressible navier-stokes equations. *Journal of Computational Physics* 1985;59(2):308 –23. URL: http://www.sciencedirect.com/science/article/pii/0021999185901482. doi:http://dx.doi.org/10.1016/0021-9991(85)90148-2.
56. Rhie C, Chow W. Numerical study of the turbulent flow past an airfoil with trailing edge separation. *AIAA journal* 1983;21(11):1525–32.
57. Felten FN, Lund TS. Kinetic energy conservation issues associated with the collocated mesh scheme for incompressible flow. *Journal of Computational Physics* 2006;215(2):465 –84. URL: http://www.sciencedirect.com/science/article/pii/S0021999105004997. doi:http://dx.doi.org/10.1016/j.jcp.2005.11.009.
58. Balcázar N, Rigola J, Castro J, Oliva A. A level-set model for thermocapillary motion of deformable fluid particles. *International Journal of Heat and Fluid Flow* 2016;62(Part B):324 –43. URL: http://www.sciencedirect.com/science/article/pii/S0142727X16301266. doi:https://doi.org/10.1016/j.ijheatfluidflow.2016.09.015.
59. Termo fluids s.l. http://www.termofluids.com/; .
60. Gutiérrez E, Favre F, Balcázar N, Amani A, Rigola J. Numerical approach to study bubbles and drops evolving through complex geometries by using a level set - moving mesh - immersed boundary method. *Chemical Engineering Journal* 2018;349:662 –82. URL: http://www.sciencedirect.com/science/article/pii/S1385894718309240. doi:https://doi.org/10.1016/j.cej.2018.05.110.
61. Amani A, Balcázar N, Naseri A, Oliva A. A study on binary collision of droplets using Conservative Level-Set method. In: *6th European Conference on Computational Mechanics (ECCM 6)- 7th European Conference on Computational Fluid Dynamics (ECFD 7)*. Glasgow, UK; 2018:11–15 June.

62. Cox RG. The deformation of a drop in a general time-dependent fluid flow. *Journal of Fluid Mechanics* 1969;37(3):601–23. doi:10.1017/S0022112069000759.

63. Grace HP. Dispersion phenomena in high viscosity immiscible fluid systems and application of static mixers as dispersion devices in such systems. *Chemical Engineering Communications* 1982;14(3-6):225–77. URL: https://doi.org/10.1080/00986448208911047. doi:10.1080/00986448208911047. arXiv:https://doi.org/10.1080/00986448208911047.

64. Vananroye A, Cardinaels R, Puyvelde PV, Moldenaers P. Effect of confinement and viscosity ratio on the dynamics of single droplets during transient shear flow. *Journal of Rheology* 2008;52(6):1459–75. URL: http://dx.doi.org/10.1122/1.2978956. doi:10.1122/1.2978956. arXiv:http://dx.doi.org/10.1122/1.2978956.